DIRECT DETECTION OF NON-METALLIC INCLUSIONS
IN MOLTEN IRON

by

Selçuk Kuyucak

Department of Mining and Metallurgical Engineering
McGill University
Montreal, Canada
August, 1985

A Thesis Submitted to the
Faculty of Graduate Studies and Research
in Partial Fulfilment of the Requirements for the Degree of
Master of Engineering

ABSTRACT

Inclusion content of a steel has been closely linked to the quality of its product. In evaluating steel quality, emphasis has been shifting recently towards using particle size distributions of inclusions and concentration of inclusions above a critical size rather than total inclusion contents as a measure of steel cleanliness.

In the work presented, an instrument that detects and counts inclusions greater than about 20 microns in molten iron on a one to one basis has been developed and tested. The method depends on an electrical sensing zone principle (or the resistive pulse technique) to provide both concentration, and particle size distribution, of suspended inclusions, through direct sampling of the molten metal.

RESUME

La proportion d'inclusions contenue dans un acier a été corrélée de façon précise à la qualité de son produit. Récemment, l'évaluation de la qualité d'un acier s'est tournée vers l'étude de la distribution de taille des particules et vers la concentration des inclusions plutot que vers le contenu total en inclusions comme mesure de la propreté d'un acier.

Dans le présent travail, un instrument capable de détecter et de compter les inclusions supérieures à 20 microns une par une dans le fer liquide a été développé et testé. Cette Méthode utilise le principe d'une zone sensible au courant électrique (technique du pic de résistivité) et détermine à la fois la concentration, la dimension et la répartition des inclusions, et ce à l'aide d'un échantillonage direct du métal en fusion.

ACKNOWLEDGEMENTS

I would like to thank Prof. R. I. L. Guthrie for useful discussions and for the faith he showed in this project, and to Dr. L. Gourtsayannis for the many tips he gave in designing our instrument and running our experiments.

My special thanks are due to our technicians, Frank Sebo for intelligently building the general structure of our measuring probe and for helping to perform the experiments, to Martin Knoepfel and Bruno Grondin for putting 'impossible' pieces together.

I would also like to thank Hidemasa Nakajima, fellow student in our group, for alerting me to the dependence of voltage pulses on the total potential drop across the electrodes in equation (9).

The research project was primarily funded by grants from American Iron and Steel Institute, and Energy, Mines and Resources of Canada.

Finally, I would like to thank McGill Computing Center for providing the funds to cover the costs of word processing and graphics.

CONTENTS:

LIST OF SYMBOLS

B	Magnetic flux density, Wb/m^2
(C_D)	Discharge coefficient
C_p	Heat capacity, J/kg
d	Particle diameter, microns
D	Orifice diameter, microns
E	Electrical potential gradient, V/m
E_f	Specific mechanical energy loss of a fluid, J/kg
f_i	Henrian activity coefficient of solute 'i'
G	Gibb's free energy, J/g-mol
G°	Standart free energy, J/g-mol
h_i	Henrian activity of solute 'i'
I	Electrical current, amperes
N_d	Number of inclusions greater than size d, g^{-1}
$\bar{N}_d$	Inclusion population density at size d, $g^{-1}.\mu m^{-1}$
P	Pressure, Pa
P(r)	Probability of having r number of particles in a given sample
R	Electrical resistance, Ohms
R	Universal gas constant, 8.3 J/°C.g-mol
(Re)	Reynolds number
S	Volumetric rate of heat generation, W/m^3
t	Time, seconds
T	Temperature, °K
$\bar{u}$	Average velocity at a cross-section, m/s
V	Electrical potential, Volts
V_d	Volume fraction of inclusions greater than size d, ppm
$\bar{V}_d$	Volume fraction density of inclusions at size d, $ppm.\mu m^{-1}$

V_t	Total volume fraction of inclusions, ppm
α	Kinetic energy correction term for a velocity profile
α	Volume of a sensing zone, mm^3
ϵ	Average number of paricles within a given size range in a given sample
ι	Current density, A/m^2
μ	Viscosity, Pa.s
μ	Magnetic permeability, H/m
μ_0	Magnetic permeability of free space, $4\pi x10^{-7}$ H/m
ν	Kinematic viscosity, m^2/s^2
ρ	Density, kg/m^3
ρ_e	Electrical resistivity, Ω.m
σ	Surface tension, J/m^2

1. INTRODUCTION AND BACKGROUND

1.1. Classification of Second Phase Particles in Steel

Second phase particles are so much a part of a steel matrix that because of their inevitable presence, steel is best described as being a composite product. For the purposes of classification however, second phase material has three entry points into the product matrix:

1. Primary Products: This refers to the formation or entrainment of second phase particles when the steel is molten. Many of the non-metallic inclusions are formed at this stage. Schematically, inclusions form in situ as a result of de-oxidation following the steelmaking operations. When the de-oxidiser is added to molten steel, it has a higher affinity for oxygen than liquid iron, and consequently removes much of the dissolved oxygen by forming second phase oxide precipitates. The resulting inclusions are then said to be indigeneous. Exogeneous or 'formed out of' products, on the other hand, include entrained particles from eroded refractory or mixed-in slag. Recently, the entrainment of mold powders in molten steel during continuous casting operations have been receiving particular attention (1).

2. Secondary Precipitates: Solid iron dissolves negligible amounts of oxygen and sulphur. Thus, precipitates of these arise because of solute enrichment during solidification, when the balance of oxygen and sulphur are converted into non-metallic

oxide and sulphide particles.

3. Tertiary Precipitates: These can occur during the transition of austenite to ferrite when the solid solution of carbon and nitrogen in steel becomes supersaturated, and carbides and nitrides or their combinations are nucleated and precipitated as a second phase product. The formation of cementite by way of eutectoid reaction could be cited as an example in this class of precipitating compounds. These can often be metallic in character. Other precipitates such as aluminum, titanium, vanadium and niobium carbonitrides are usually very fine and give rise to improved mechanical properties as a result of their grain refining action. Unlike primary inclusions, their presence is desirable and their controlled precipitation is the subject of much research (2,3).

Hence, from the foregoing, an inclusion may be defined as those second phase particles which are non-metallic in character, and which usually have deleterious effect on the mechanical properties of steel. An elucidation of this definition in relation to other second phase particles is given in Table 1. Because of their importance, inclusions and 'steel cleanliness' have been the subject of a number of symposia and conferences (4-11).

Table 1
Second Phase Particles in Steel and Definition of Inclusion

Primary Particles

Those that form in liquid steel

Secondary Particles

Those that precipitate from supersaturated liquid during solidification as a result of solute enrichment.

inclusion

is a primary or secondary particle greater than a critical size that have detrimental effect on properties

Tertiary Particles

Those that precipitate from a supersaturated solid solution during austenite to ferrite transition

1.2. De-oxidation and De-sulphurisation of Steel

Molten iron dissolves a significant amount of oxygen: 2100 ppm in equilibrium with wustite at a partial oxygen pressure of 5×10^{-9} atmospheres. It also dissolves an unlimited amount of sulphur, 1% of which would be equilibrium with a partial sulphur pressure of 5×10^{-8} atmospheres at the melting point of iron, 1535°C (12). In the absence of other solutes, all dissolved oxygen and sulphur converts to secondary precipitates of iron oxides and iron sulphides during solidification. Wustite (FeO) separates first, while sulphur remains until the stoichiometric composition of FeS is reached in a final film of liquid around the dendritic grains of iron. Both precipitates then solidify, at 1370 and 1195°C, respectively (13).

Liquid steel containing dissolved oxygen and no deoxidiser agents may therefore be considered 'clean' until it starts to solidify. Solute enrichment of oxygen, together with residual carbon and other solute elements, then results in the formation of pinholes, blowholes and other secondary precipitates. The purpose of de-oxidation and de-sulphurisation is to remove the major part of any dissolved oxygen and sulphur by forming second phase particles and then removing these from the molten steel by flotation or entrapment to the refractory lining walls of the container (e.g. ladle).

Continuous casting requires steel to be "killed" for the operation to be succesful (i.e. break-outs). The ever increasing use of continuous casting, even for sheet products which in the past have traditionally been manufactured via semi-killed ingots for ensuring good surface quality, means that almost all bulk steels currently being manufactured are completely deoxidised. This deoxidation is effected in the ladle, first by additions of manganese and silicon which bring the dissolved oxygen content down to about 50 ppm, and then by additions of a stronger deoxidiser such as aluminum reduce oxygen even further, to a few ppm. The total oxygen content of a steel is however, rarely less than about 10-20 ppm because of the presence of deoxidation products that have not yet left the molten steel. If adequate protection is not taken to prevent ingress of air around teeming streams, emptying from ladles, atmospheric oxygen can dissolve in molten iron and react with solute deoxidisers to create more inclusions.

Very little dissolved oxygen is left for secondary precipitation once a steel has been fully deoxidised, so that almost all oxide inclusions encountered in solid steel come from primary sources.

As for desulphurisation, the trend in today's steelmaking practice is to remove a large portion of sulphur prior to the steelmaking step, thus sulphur is removed from molten iron in the torpedo car, where 'low' temperatures (1350°C) and a reducing environment (high carbon) are thermodynamically more favourable for sulphide formation. Desulphurisation is often carried out using powder injection of desulphurisers such as calcium carbide, $CaO-CaCO_3$, Mg etc. Wire injection of desulphuriser metals such as magnesium is also being tried in North America, and recently in Japan, as opposed to powder injection (14).

If hot metal is not treated for sulphur prior to steelmaking, some sulphur removal can still be effected in the converter. Untreated steels in ladles then typically contain 300 ppm of sulphur. Most sulphides form as secondary precipitates and, if some form of modification is effected by sufficient additions of manganese to prevent formation of iron sulphides (and, 'hot shortness') or by additions of rare earth metals to produce globular sulphides for improving 'through-thickness notch toughness'; much of their deleterious effect on properties can be attenuated.

Although a moderate level of sulphur is permissible for most purposes (e.g. 200 ppm), it is unsuitable for some steel grades such as cold weather pipeline steels, where stringent notch toughness requirements for low ductile/brittle transition temperatures and high upper shelf energies are required. For these steels, current sulphur levels are kept below 10 ppm.

Because of the possibility of sulphur pickup from carry-over converter slag, this level of sulphur is not obtained directly in the hot metal, but the final lowering of sulphur is obtained by secondary refining (e.g. via the T. N. Process).

Desulphurisation in the ladle is more difficult than deoxidation, since elements having an affinity for sulphur have an even greater affinity for oxygen. Japanese and West German steel companies were among the first to initiate powder injection for the production of extra low sulphur pipeline grade steels. To effect this, steel is first strongly deoxidised under a reducing basic slag, after which injection of strong desulphurising powders, such as calcium silicide in the T. N. process is performed with subsequent mixing by argon stirring for periods of up to 30 minutes (15). Dissolved sulphur can combine directly with the desulphuriser or exchange places with oxygen in the deoxidation products.

A sulphur probe like an oxygen probe to measure the dissolved sulphur content would have been very useful in this respect. However, a solid sulphide electrolyte, stable at steelmaking temperatures and its environment, and selective to dissolved sulphur atoms, is yet to be discovered (16).

The foregoing remarks imply that any extensive desulphurisation results in the presence of primary sulphide inclusions. Any such sulphide particles remaining in the liquid can affect a steel's performance for certain applications. As such, their detection, along with oxide inclusions, is needed for quality control.

1.3. Inclusion Nucleation and Growth

When liquid steel is mixed with a deoxidiser, deoxidation products nucleate either homogenously or heterogenously, the matter having been of some debate. But large number of nucleation sites exist; direct measurements put the value to somewhere between 10^3 to 10^5 nuclei per cubic mm (17). As a result, growth by diffusion can be very fast. Calculations (18) and experimental evidence with an oxygen probe (17) give a time scale of a few seconds, after which oxygen in the vicinity of a deoxidiser is depleted to its thermodynamic equilibrium value so that any deoxidation product could only grow to about 1 or 2 microns. Mixing of the deoxidiser in solution in fact, takes more time, depending of course on bath size and mixing conditions. Again, using an oxygen probe in a small unstirred bath, thermodynamic equilibrium has been shown to be attained in a matter of few minutes (19).

Today, it is commonly suspected that further growth of deoxidation products occurs through some form of coagulation. In fact, oxide inclusions with higher interfacial energies such as alumina grow faster and produce more macro-inclusions (greater than 40 microns), than do wetting silicate oxide inclusions. As this phenomenon cannot be explained by diffusional growth alone, it tends to support the possibility of 'in-melt' coagulation.

The effect of inclusion growth is two-sided in the sense that both the likelihood of inclusion removal and the likelihood of encountering a macro-inclusion within the steel matrix increases. Plant experience indicates that the disadvantage of the latter usually dominates. In the production of bearing steels for instance, where oxide inclusion contents have a critical effect on properties, their production by way of aluminum deoxidation, as opposed to solely Mn-Si deoxidation, produces steels of usually inferior quality and of unpredictable cleanliness (20).

It would have been desirable to avoid aluminum as a deoxidising agent altogether but its grain refining action and the removal of nitrogen from solid solution as a result of tertiary nitride precipitates is necessary for imparting other qualities to the steels. Consequently, efforts have been concentrated on the removal of primary alumina inclusions, or their fluxing by lime or calcium-silicon injection.

1.4. Effect of Inclusions on Properties and Definition of Steel Cleanliness

Much has been written about the effects of inclusions on the mechanical properties of steel. The subject is complex and depends on the size, shape, distribution, and constitution of inclusions. Constitution, in this respect, is important as it determines deformability, and hence, the final shape after hot working, also matrix cohesion, internal stresses caused by differential thermal expansion and susceptibility to void formation (21).

Complexity arises because, although most inclusions are deleterious to some extent, some can impart improved properties, e.g. sulphide particles are used as aid for the machinability of steels, or inclusions can be used to counteract the deleterious effects of others, e.g. dampening the crack nucleation effect of oxides in steels by the surrounding sulphides, resulting in improved fatigue strength and buffered susceptibility to hydrogen induced cracking in the heat affected zone of weldments (22).

An excellent review exists for the quantitative effects of inclusions (second phase precipitates) formed from impurity elements in liquid steels such as phosphorus, sulphur, nitrogen, carbon and oxygen, on final properties such as ductility, notch toughness, susceptibility to hydrogen induced cracking, stress corrosion cracking and pitting corrosion, fatigue strength, hot workability, deep drawability, wire drawing capability, machinability and weldability, for various types of steel designed for different end uses in reference (23).

Most primary inclusions in the ladle are of the oxide or the oxysulphide type, and since their detection forms the basis of the present work, a brief review of their effect on the properties will be relevant. Oxide inclusions are non-deformable at room temperature and have an important effect on the fatigue strength as crack nucleaters. Other deleterious effects particular to oxide inclusions include susceptibility to hot working defects such as seams because of large oxide inclusions near the surface of a billet (24), lack of polishability which is important in some applications such as lens molds used for forming plastics (25) and lack of surface quality and susceptibility to pitting corrosion in stainless steel sheets (26,27).

Usually inclusions greater than a critical size are largely responsible for impaired properties. The critical size varies according to the property looked into and have only been vaguely defined for most properties, but is likely to be an important parameter in the assessment of steel cleanness (28). Current agreement to quantify steel cleanliness with regards to inclusions has been towards a statistical treatment: clean steel is regarded as one where the probability of finding inclusions larger than a critical size at a critical site is small.

This statistical approach was first used by Nordberg to develop a model showing how the fatigue limit could be predicted from an inclusion size distribution curve (29). In an earlier study, Wojcik et al. use the size distribution curve to predict susceptibility of steel billets to surface defects during hot working operations (24). In this regard, size distribution curves emerge as important tools in quantifying steel cleanliness.

In conclusion, numerous inclusions form in liquid steel following deoxidation and desulphurisation operations. Their usually deleterious effects on properties depend on their type, size and concentration. Consequently, a great deal of effort has been focused on developing methods to quantify inclusion content of a steel in various stages of its processing. A review of these methods will be dealt with in the next chapter.

2. REVIEW OF INCLUSION DETERMINATION TECHNIQUES

2.1. Chemical and Physical Methods for Total Volume Fraction of Inclusions

As oxygen and sulphur are virtually insoluble in solid iron, total oxygen and sulphur contents give the first indication of the inclusion content of a steel. If the constituent oxides and sulphides are known, the volume fraction of inclusions can then be calculated by use of equation (56) in Appendix II. A number of commercial instruments exist for fast and accurate chemical determinations, whose principles depend on vacuum or inert gas fusion followed by reduction of combined oxygen to carbon monoxide by a graphite crucible for total oxygen and combustion to sulphur dioxide for total sulphur (30). A physical method also exists for total oxygen where neutron activation of combined oxygen and subsequent analysis by a radioactivity measurement is employed. The sample size used in this method can be considerably larger, a few kilograms compared to 1-5 grams used in the chemical methods.

A novel method has also been developed for special alloys where button samples (typically 680 grams or 1.5 lb) are produced in a water cooled copper mold by remelting a weighed sample drop by drop under vacuum using the electron beam of an E. B. furnace (31). Because of surface tension and gravity, inclusions are amalgamated as a raft on top of the molten button. By measuring the dimensions of the 'raft', the volume fraction of inclusions can be determined directly (31). The method applies to relatively clean steels (less than 100 ppm volume fraction of inclusions) and is probably selective with respect to inclusion type and size.

Although these methods give a first measure of cleanliness, all, with the exception of electron beam method, give no idea of the size, or number, of inclusions. As explained in Section 1.4 however, greater emphasis is presently being placed on this in quantifying steel cleanliness.

2.2 Methods Based on Surface Examination

Among these, macroscopic and microscopic techniques are commonly used by industry. Macro-examination attempts to reveal particularly large inclusions. As with all methods that depend on surface examination, the method suffers from the limited sample volume possible via this technique. To overcome statistical sampling problems, large surface areas have to be examined. Observation is aided by the relative ease of sample preparation since machined and ground surfaces are quite sufficient to allow inclusions as small as 0.4 mm long to be detected. Highly polished surfaces are therefore not necessary, as they are with microstructural analysis. An alternative approach to macroscopic examination is to view fresh fracture surfaces. These are examined in locations where inclusions are expected to be more concentrated. The American Society for Testing and Materials describe four testing procedures for macro-examination of steel samples (32):

1. Macroetch Test: Machined sections are etched with hot hydrochloric acid and examined visually or at low magnification for the presence of inclusions greater than about 0.4 mm.

2. Fracture Test: As the name implies, a hardened sample is fractured and the surface is examined for inclusions greater than 0.4 mm.

3. Step-Down Method: A straight cylindrical sample is machined to specified diameters below the surface in a stepwise fashion and is examined for inclusions 3.2 mm in length or longer.

4. Magnetic Particle Method: This is used to increase the sensitivity of the stepdown method for ferromagnetic steels. The machined sample is circularly magnetised by passing a heavy D.C. current and is then treated with a magnetic powder. Discontinuities as small as 0.4 mm in length create magnetic leakage fields which then attract the magnetic powder and outline the inclusions.

The results of such macro-examinations can be expressed in terms of frequency and severity which is the weighted sum of frequency results where larger inclusions have more weight. This enables some sort of size distribution of macro-inclusions to be constructed.

Microscopic examination requires a polished surface and because of magnification (typically 100x), the scanned area is small (0.5 mm²). Hence, measurements have to be made on a number of fields, so as to increase the sample size. The total area covered typically varies between 160 to 1000 mm² (32,20). This, of course, makes the method very laborious. To ease the burden of these manual determinations, a number of standard charts have been drawn, against which the microscope image is compared and a cleanliness value is directly assigned. Some of these methods consider only the size of inclusions (the Fox count), whereas others also analyse for their type (JK counts). Unfortunately results are operator dependent and this has been demonstrated to have a large effect on the accuracy (repeatability) of results (33).

Direct methods of inclusion assessment based on classical quantitative metallography proves to be more accurate but prohibitively laborious even for research work. This led to the development of Automatic Image Analysers, based on optical or electron microscopy where such quantitative factors as area fraction, shape factor and size distribution of inclusions can be measured considerably faster (34,35). Since their first commercial introduction in 1963, considerable development has taken place in these instruments, especially in ensuring the repeatability of the results by overcoming the earlier difficulties of threshold adjustment (36). Because of their increased reliability, automatic image analysers are now more popular, and as practiced in Japan, surface areas as large as

10x10 cm can be examined overnight so as to ensure adequate sampling (37). However, the instruments are expensive and this prohibits their universal use.

The sample size of a surface examination depends on the estimated thickness of the surface examined. This in turn depends on the inclusion size. Hence, the sample size may be considered to increase linearly with inclusion size for a given area. But inclusion population decreases much more rapidly than a linear relation with increasing size; therefore, larger areas must be covered for determining macro-inclusion distributions.

A very early study showed that the area fraction of a phase is also the best estimate of its volume fraction (38). This fact enables the estimation of volume fraction of inclusions from surface area examinations.

2.3. Non-Destructive Testing

Methods of N. D. T. depend on the through transmission attenuation of X-rays using radiography measurements and recently more so on ultrasonics using pulse-echo signals, lamb waves, and in some cases through transmission attenuation measurements. They are widely used for detecting relatively large flaws in solids that may be caused by macro-inclusions, gas voids or other foreign material.

The methods are fast enough and have been successfully automated, so that ultrasonics can be used for the on-line inspection of all quality products (e.g. seamless or E-W pipes). However, some difficulty still exists in the interpretation of detected signals (39,40).

The development of non-contact methods such as Electro-Magnetic Acoustic Transducers (EMAT) or pulsed lasers, and laser interferometry, to generate and detect acoustic waves, also hold promise for the inspection of hot blooms and slabs at temperatures in excess of 1000°C (41).

The low cost of computing is now making computer aided tomography possible: this refers to the reconstruction of 2-D images of cross-sections through attenuation measurements (42). Tomographic images are much more accurate with respect to location, shape and size of flaws, than the classical radiographic or ultrasonic images.

2.4. Chemical Extraction of Inclusions and Residue Analysis

Techniques for the extraction of acid insoluble inclusions from steels has been known since the early 1930's (43). Subsequent improvements to the method now allow reliable extraction of most second phase particles from iron matrix. Halogens in organic solvents are considered the best means for dissolving out the steel matrix to release the oxide inclusions (43). The residues can than be analysed by various analytical techniques (e.g. X-ray diffraction, spectrochemical analysis and optical microscopy).

One version of the method, most interesting to the present work, is the size distribution determination of such residues by an aqueous Coulter Counter device. This technique has been refined to include macro-inclusions, as well as micro-inclusions, by Flinchbaugh (44,45). Its use has revealed important information on the typical number of growing nuclei and typical size distribution of inclusions in deoxidised steels (45-48). The method was popular as a research tool until the early 1970's; automatic image analysers are currently more popular, as they are capable of extracting similar information as the residue analysis with less labour (37).

2.5. On-Line Techniques for Molten Steel Currently being Developed

There is a demand for on-line methods to detect flaws and inclusions in steel so that corrective action can be taken as early as possible. The detection of non-metallic inclusions in liquid steel represents the ultimate in this respect. Some of the above mentioned methods can be employed to this end, such as U. S. Steel Corporation's automatic image analyser, coupled with a scanning electron microscope to evaluate area fraction of inclusions in solid steel samples. The method is slow however, particularly as steels become more clean, an increasingly larger area must be sampled for statistically significant results (50).

As already mentioned, the development of non-contact ultrasonic methods is quite interesting for on-line inspection of the preliminary stages of processing, and a commercial EMAT system has been reported to have already been operated in Nippon Steel for several years in a continuous casting process (41). However, these methods are inherently limited to large flaws and surface cracks.

The use of metal wave guide extensions and ceramic sleeve contactors, also makes the ultrasonic detection of inclusions in molten metals at elevated temperatures possible. The technique itself was patented in the late 1940's. It was developed considerably for aluminum by the Reynold's Aluminum Co. (51) and further development for molten iron is currently taking place in the University of Toronto (52). But again, common to ultrasonic testing, the large particle detection limit restrains the usefulness of the method for inclusion detection.

In line with all other instruments that depend on wavelength for detection, it is claimed for ultrasonic detection that individual particles greater than 1/2 the signal wavelength can be detected by pulse-echo measurements (51). Signal frequency cannot be increased presently to more than about 10 MHz because of a rapid increase in signal attenuation by the metal waveguides, while the wavelength of sound in molten steel would be in the order of 500 microns for the typical sound velocities encountered. Consequently, only particles greater than about 250 microns would be detected.

Perhaps a more useful approach would be to take through transmission attenuation measurements where particles as small as 1/10th of the signal wavelength are claimed to contribute to sonic attenuation (51). This would be relatively fast and would, in theory, give the overall volume fraction of macro-inclusions. However, there seems to be much development work before an instrument could be realised for quantitative measurements in molten iron and more so in steel (52). Even then, a detection limit of only 50 microns would be possible provided a sufficient concentration of inclusions above this size exists.

Another recent innovation with regards to inclusion detection in molten metals has been the application of the resistive pulse technique to construct a Coulter-Counter-like device for aluminum, and also for other lower melting point metals. The research was initiated at McGill in 1980 because of the lack of a good analytical tool for the on-line detecion of deleterious particles in liquid aluminum. An instrument named "LiMCA" (Liquid Metal Cleanliness Analyser) has been developed and fully tested in many casting centers of a major aluminum producer (53). The instrument is capable of giving information on aluminum cleanliness in the form of total number and size distribution of particles in a given sample volume with a detection limit at 20 microns. Its application to molten iron forms the basis of the present thesis, as outlined in the following chapters.

Automatic image analysers, pulse-echo ultrasonic techniques, and resisitive pulse counters may be considered as sensing zone instruments in the sense that they analyse characteristic samples one at a time (54). Conceptually, a classification for the above may be made as optical, sonic and electrical sensing zone instruments respectively where similar counting statistics and coincidence effects apply in their operation as discussed in Chapter 7.

The great advantage of the resistive pulse counter over the others is a combination of its speed and a good detection limit: with the instrument that will be described for instance, the residence time of individual samples at the sensing zone is only 0.3 ms and, at a detection limit of 20 microns, 50 grams of steel sample can be readily analysed in one minute.

3. BACKGROUND TO THE SYSTEM

The resistive pulse counting technique was originally developed by Dr. Wallace Coulter (55,56) in the 1950's for automatic counting and size analysis of blood cells. Since then, it has also been extended to the field of powder technology for particle size distribution measurements of powders suspended in aqueous media. With regards to measuring non-metallic inclusions in steel, examples of its use include size distribution measurements of inclusions in the extracted residues from steels as discussed in Section 2.4. More recent studies of inclusion behaviour in ladles and tundishes using water models have also made use of this electrical sensing zone technique (57,58).

3.1. Principle of Operation in Molten Metals

The resistive pulse counting technique depends on forcing the liquid metal into an electrically non-conductive sampling tube (the sampling cell) through a small orifice (the sensing zone). A current path is simultaneously established through the orifice by the use of suitably immersed electrodes in- and outside the tube. Each time an electrically non-conductive second phase particle enters the orifice, a slight increase in voltage occurs across the electrodes because of the momentarily increased orifice resistance. The amplitude of the voltage pulse is, to a first approximation, proportional to the volume of the particle. By measuring and counting each pulse via a suitably arranged electronic apparatus, it is then possible to obtain a direct histogram of particle size versus particle frequency for a given volume of liquid metal.

3.2. Relationship Between Particle Size and Magnitude of Resistive Pulse

Consider the resistive pulse ($\Delta R=R_1-R_0$), caused by the presence of a spherical, non-conducting particle of diameter (d) in the middle of a right circular cylinderical orifice of diameter (D) and length (L), (Figure 1). Even for this simple geometry there is no simple analytical solution valid for all values of (d/D) ranging from 0 to 1. This is due to the distortion of electric field streamlines around the particle resulting in a non-uniform radial distribution of current. Ohm's law in its simple differential form:

$$\delta R = \rho_e \cdot \delta x/A(x) \tag{1}$$

is, as a result, not precise in predicting the new resistance of the orifice. A complete solution to such problems requires solving the Laplace's equation for electric field potential in which both sphere and cylinder boundaries are insulating (59).

Simple solutions do exist however, for the limiting cases when (d/D) tends either to 0 or 1. Since at the detection limit dmin, (d/D) is small, the former approximation is of particular interest. As shown by DeBlois and Bean (59), an expression for ΔR can be derived by making use of Maxwell's approximation for the

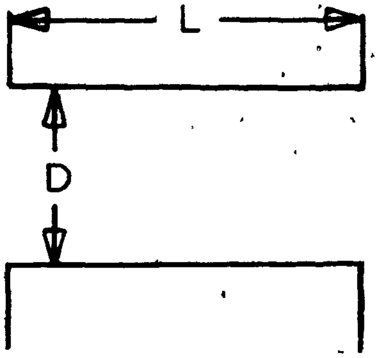

(A) RIGHT CYLINDRICAL ORIFICE WITHOUT PARTICLE

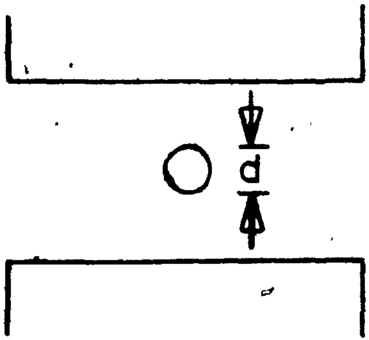

(B) WITH A SPHERICAL PARTICLE IN THE MIDDLE.

RESISTANCE CHANGE IS GIVEN BY EQUATION (3).

Figure 1 Geometry of the orifice used in the derivation of equation (2) for the change in resistance caused by a symmetrically placed spherical particle and the correction factor in equation (4).

effective resistivity of a conducting fluid containing a dilute suspension of insulating spheres. The derivation is given in Appendix I, and the result is:

$$\Delta R = \frac{4}{\pi} \frac{\rho_e d^3}{D^4} \qquad (2)$$

This expression indicates that the resistive pulse is proportional to the volume of the particle and is independent of the length of the orifice. Although equation (2) holds for small values of (d/D), exact values of ΔR are only greater by 2% at d/D=0.3 and 5% at d/D=0.4 (60).

For large values of (d/D), a correction factor needs to be incorporated into equation (2) such that:

$$\Delta R = \frac{4}{\pi} \frac{\rho_e d^3}{D^4} \cdot F(d/D) \qquad (3)$$

Such correction factors have been calculated via numerical solutions and have been tabulated for the case of an insulating sphere placed in the middle of a long, right circular cylindrical orifice using a hydrodynamic analogy (60). They are also shown to give an excellent fit to the following empirical equation (61):

$$F(d/D) = 1 / \{1 - 0.8(d/D)^3\} \tag{4}$$

with an error of less then 1% at (d/D=0.8).

To find a value for the voltage change, equation (3) would normally have been multiplied by the circuit's current. However, a close examination of the Ohm's law reveals that the potential drop across the electrodes over which the voltage pulses are detected also has some significance. Referring to Figure 2 and applying Ohm's law to the circuit shown,

$$\Delta V_{pulse} = I_1(R_E + \Delta R) - I_0 R_E \tag{5}$$

$$\Delta V_{pulse} = V_T \bullet \left\{ \frac{R_E + \Delta R}{R_E + R_B + \Delta R} - \frac{R_E}{R_E + R_B} \right\} \tag{6}$$

$$\Delta V_{pulse} = V_T \bullet \left\{ \frac{R_B \bullet \Delta R}{(R_E + R_B + \Delta R)(R_E + R_B)} \right\} \tag{7}$$

where I_1 and I_0 are currents with and without the particle, V_T is the battery's electromotiv force, R_E the total electrode, and R_B, the ballast, resistances respectively.

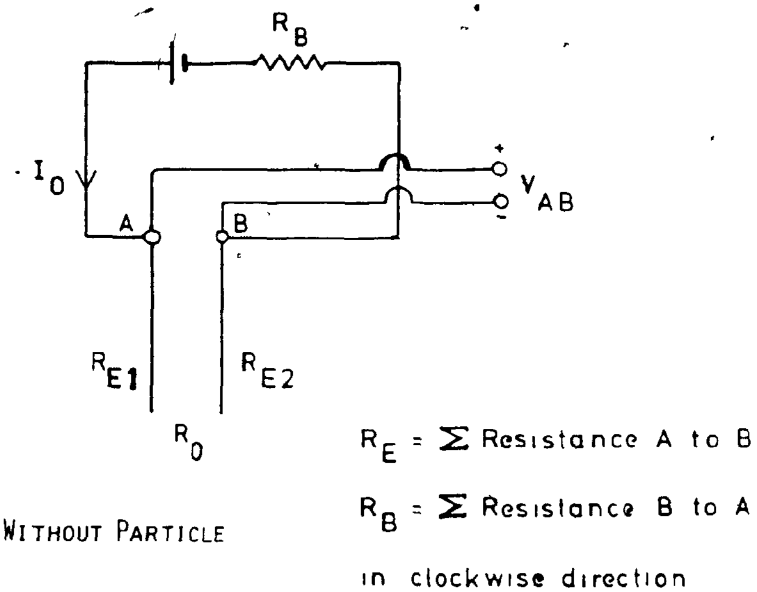

A. WITHOUT PARTICLE

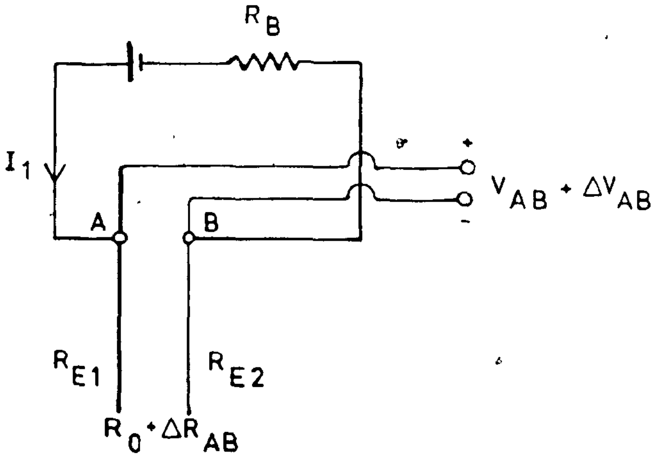

B. WITH PARTICLE

Figure 2 Circuit diagram showing the generation of a resistive pulse.

$$\Delta V_{pulse} = I_0 \frac{R_B}{R_E + R_B + \Delta R} \Delta R \qquad (8)$$

The effect was discovered fortuitously during water experiments when no resistive pulses were observed upon removing the ballast resistor. It arises because of the minute change of current as the particle passes through the orifice. Therefore the voltage pulse, ΔVpulse when written explicitly, using the potential drop accross the electrodes (VE) and neglecting ΔR in the denominator, becomes:

$$\Delta V_{pulse} = \frac{4}{\pi} \frac{V_T - V_E}{V_T} \frac{\rho_e d^3 I_0}{D^4 \{1 - 0.8(d/D)^3\}} \qquad (9)$$

In Figure 3, resistive pulse (ΔV) has been plotted as a function of particle size (d) according to equation (8) for cylindrical orifices of various diameters using the suggested currents in Table 11-(B). The plots were terminated at d/D=0.8. As can be seen from the log-log plot, the resistive pulse response increases in proportion to the cube of the particle diameter, up to almost d/D=0.4. The slope then deviates towards larger values. For spherical particles with d/D≤0.4 then, resistive pulses may be considered to be proportional to the particle volume.

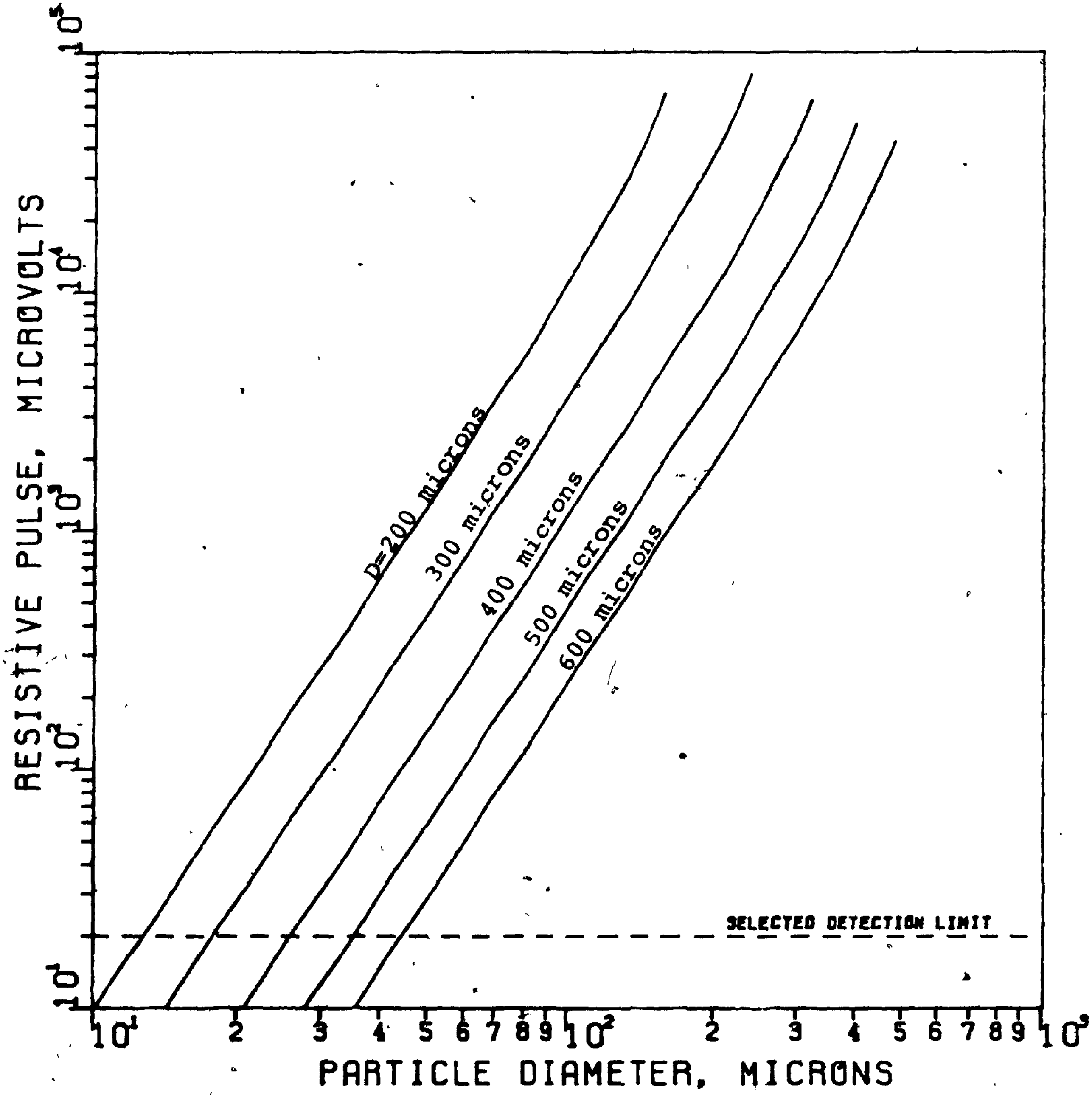

Figure 3 Resistive pulse as a function of particle size (d) and orifice diameter (D), using equation (8) and the suggested currents in Table 11-(B).

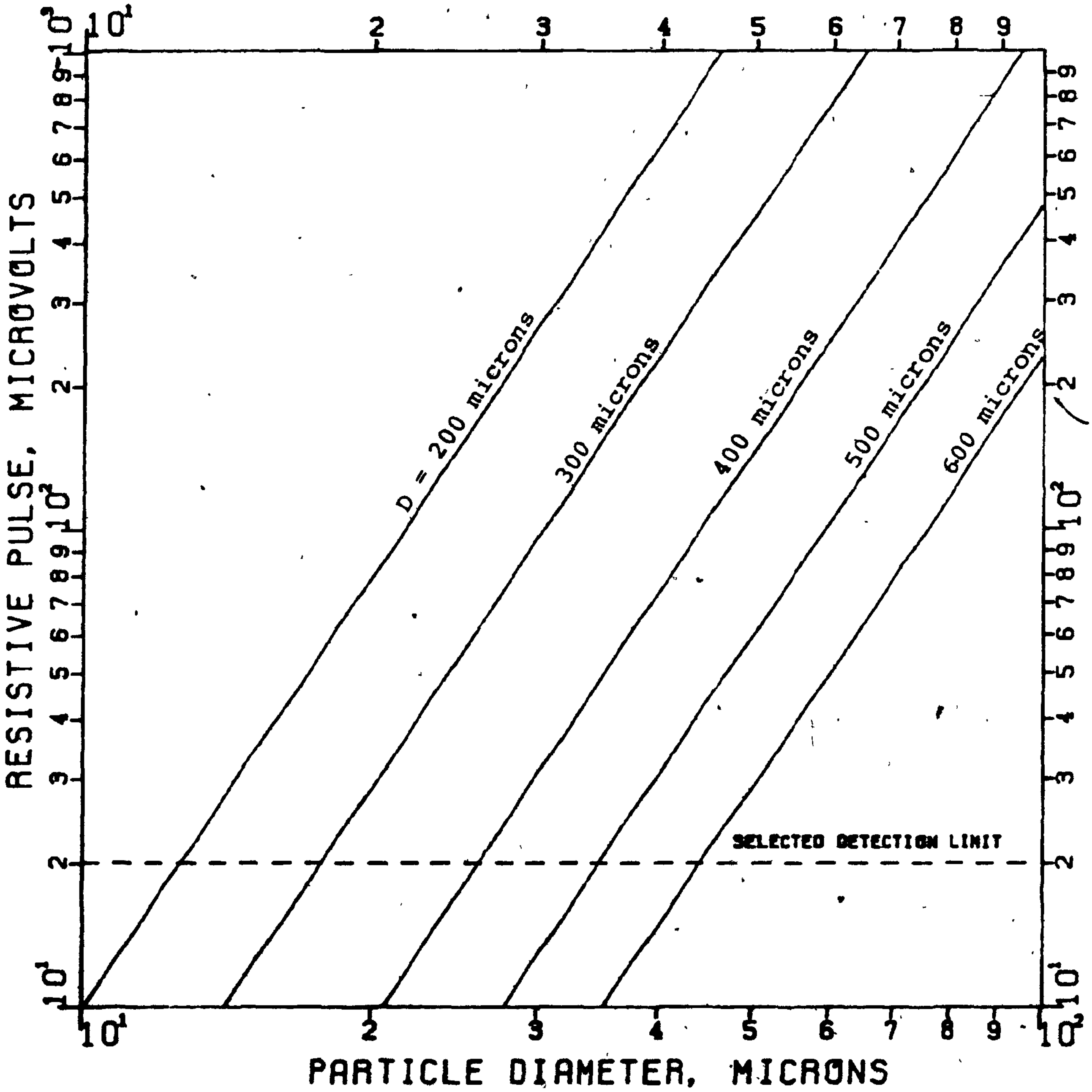

Figure 3-A Lower left quarter of Figure 3, used for converting resistive pulse voltage peaks into particle diameters.

Gradually tapered orifice is found to be an optimum shape for resistive pulse analysers. Consequently, equation (9) should be modified for the shape and also, to a lesser degree, for the length of orifice if the length is short. Although there is a one to one correspondence between (ΔV) and (d), such analytical formulations are of limited value because of the fourth order dependency of ΔV on D, consequently it is recommended in practice to calibrate the orifice with standard spheres in aqueous media.

Further complications can also arise because of off-axis trajectories and non-spherical particle shapes. These problems have been investigated by a number of researchers, Smythe (62) for instance, calculated significant increases in the value of ΔR as the particle trajectory approaches orifice wall. Higher than expected resistive pulses are the result of a non-uniform electrical potential gradient distribution at the orifice entrance and exit. For a sharp edged inlet, potential gradients increase substantially near the rim and, as a result, off-axis trajectories give rise to artefact peaks commonly named as "castle peaks" because of their turreted appearence (63). These peaks also have longer than average residence times. The effect of off-axis trajectories can be seen during the calibration of the instrument with standard spheres when the measured size distribution by ESZ instrument suggests a wider size distribution than those determined via microscopic analysis (64). The discrepency can be quantified by a Mass Balance Ratio (MBR), which is the ratio of the mass calculated by count to the mass recorded by weight. MBR's as great as 1.3 systematically occur in the standard Coulter equipment; the use of tapered orifices and some form of hydrodynamic focusing have been reported to remedy this, resulting in MBR's near unity (64,65)

The effect of particle shape has been shown to be insignificant at $d/D \leq 0.2$ when the system responds to particle volume (66). Consequently, the diameters of equivalent volume spheres or "Equivalent Spherical Diameters" (ESD), can be determined by the use of equation (9). At larger values of (d/D) however, shape factor becomes important. At ($d/D=0.4$) for instance, error involved in the use of equation (9) is in the region of 10% for spheroids of eccentricity 2 (67,68).

3.3. Comparison of the Resistive Pulse Counting Technique for Aqueous Media and Molten Metals

Although equation (2) has been shown to apply in both systems (53), the main obstacle in developing a system for metals was the million times greater electrical conductivity of the latter which would result in the generation of much smaller resistive pulses. The high conductivity of metals however, also makes it possible to pass much higher currents, greater than 10 amperes, without causing excessive heating at the orifice and to detect much smaller voltage pulses, of the order of 20 microvolts for instance, against a constant background noise of 5-10 microvolts when the wiring is properly shielded.

A comparison is made in Table 2 in terms of the properties of both media. When compared for a minimum particle size detected with a given size orifice, one finds:

$$d_{min,steel} / d_{min,water} = 2.2 - 1.4 \qquad (10)$$

showing that detection limits can be kept within the same order of magnitude.

Table 2
Comparison of Electrical Sensing Zone Instruments in Aqueous Media and in Metallic Systems

	Water (56)	**Steel**	
Electrical Resistivity	30	1.4×10^{-6}	Ωm
Typical Current	50×10^{-6}	10-40	Amperes
Detection Limit	200	20	μV

4. DESCRIPTION OF EQUIPMENT

The apparatus used was essentially the same as that of previous work on aluminum (53) and is illustrated schematically in Figure 4. The main components are now highlighted including some of the different design features from that of Doutre. These had to be adopted to overcome the corrosive, high temperature environment of molten steel.

4.1. Metal Sampling System

The sampling tube, into which the metal was drawn through the orifice, was held by a "Viton" seal O-ring inside an aluminum/brass metal coupling. It was foud that different metals made the screw threads of the assembly easier to seperate after each experimental run.

A gas port with a copper pipe extension was used to evacuate and pressurise the tube for sampling and purging respectively. The vacuum source was regulated by a 15 litre vacuum resevoir that was held between 10-20 cm Hg (13-26 kPa-g) and controlled with an accuracy of 1 cm Hg. The amount of vacuum necessary was usually controlled by the orifice size, i.e. to overcome the surface tension forces and enable the molten steel to be aspirated into the tube. Argon gas was used before insertion of the tube into steel so as to flush out any air and provide an inert atmosphere inside it. Similarly, after sampling was completed, to drain the tube under a moderate pressure

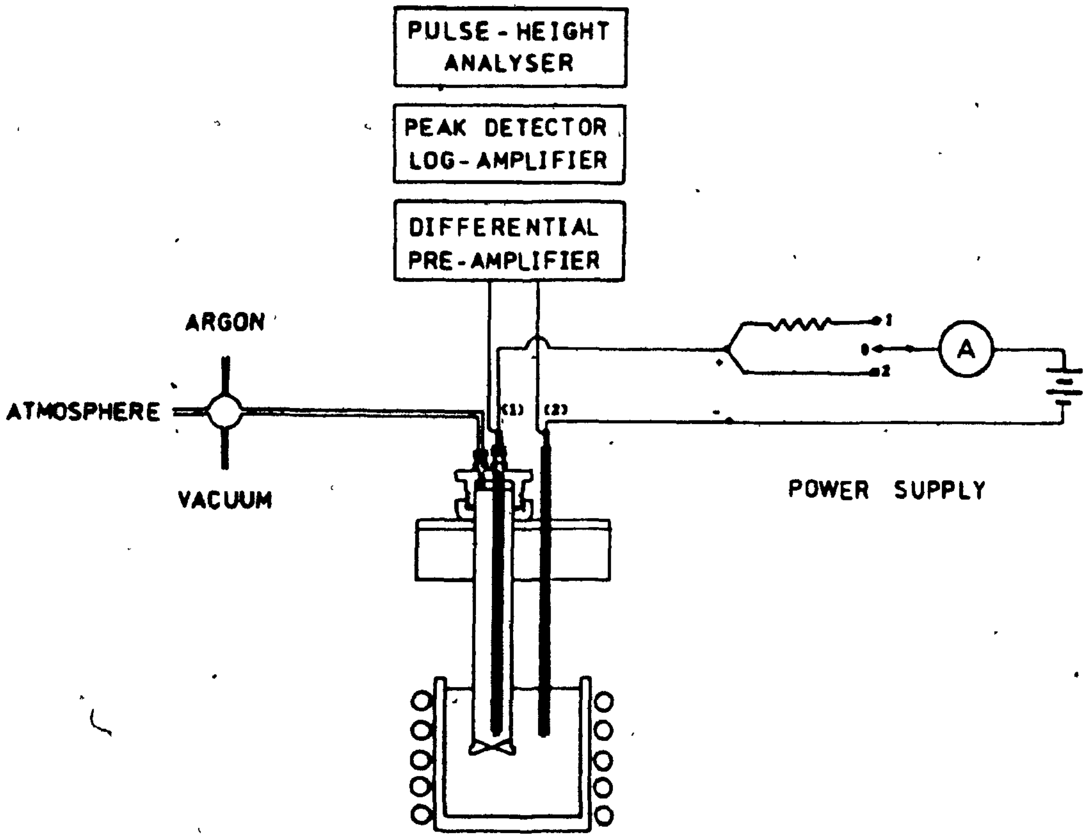

Figure 4 Schematic illustration of the resistive pulse counter used in moten iron.

(20-40 kPa-g). The volume of gas passing through the gas port was observed on a sensitive flowmeter. In the event of a blockage, positive pressure was increased up to 100 kPa-g and an alternate vacuum and pressure was applied.

Since it was necessary to change the electrodes after each experiment, they were not permanently mounted but held by compression fittings with teflon ferrules. The viton and teflon seals in the assembly were protected against thermal radiation by a 5 cm thick ceramic fibre insulation inside and outside of the sampling tube and the seals provided reasonable gas tightness during the course of experiments.

4.2. Constant Current Power Supply and Electrical Connections

As in the earlier design (53) a 6-volt lead-acid type heavy duty cart battery with appropriate ballast resistance was used as the power supply to provide ripple free current. The wiring connections were made with gauge 6 copper cables and, where possible, shielded and twisted to guard against noise pick-up. Ballast consisted of 0.5 to 1.0 ohm, 100 watt resistors mounted in parallel to maintain a current level in the proximity of 5, 10, 20 or 40 amperes. The exact value of the current was observed on a 0-100 amp DC ammeter. All electrical connections were soldered except at the electrode ends where lugs were used and connections were made by compression.

Since it had been found beneficial with aluminum, a system for short circuiting the ballast resistor with 6-V or 12-V battery potentials was also incorporated to produce a high current density and localised heating at the orifice and was used in trying to achieve a steady signal baseline.

4.3. Electronic System for Voltage Pulse Detection and Measurement

As illustrated in Figure 4, to detect and measure the voltage pulses generated by the passage of a particle through the orifice, potentials at the ends of the current carrying electrodes were fed into an oscilloscope input along teflon coated RG-59 equivalent coaxial cables recommended for high temperature applications. The oscilloscope used was a Tecktronix model 5223, a 10 MHz digitizing storage (memory) scope equipped with a model 5A22N differential amplifier and a model 5B10 digital time base. The oscilloscope permits observation of the stability of the baseline and of the voltage pulses and is also used as a pre-amplifier with a gain set at 1000.

The differential pre-amplifer is operated in the AC coupled mode where each input signal is first connected to a capacitor to eliminate the voltage drops due to resistances of the electrodes and the stable component of the orifice potential. The bandwith of the amplifier is also adjusted to the frequency of interest by the use of low and high pass RC filters, thereby removing much of the high and low frequency noise. The filters were usually set at

0.1 and 10 kHz respectively.

The preamplified signals were then fed to a Tracer-Northern model TN 1214 logarithmic amplifier which converted the 3-cycle linear 10 mV to 10 V input into a logarithmic 0 to 10 V output. This has the effect of expanding the resolution near the detection limit in the lower ranges of particle sizes.

A "sample and hold" circuit with a switch selectable pulse rise time also enables the instrument to serve as a peak detector for the Multi-Channel Analyser by holding the pulses of relatively long and approximately known duration for 3 microseconds at their peak and sending a square wave of short duration to the MCA. The pulse rise time is at most 1/2 of the residence time of the particle through the orifice which is determined by the orifice length and metal velocity, which in turn depends on the applied vacuum. For most of the present experimental conditions, particle residence time was in the region of 0.5 milliseconds, so the pulse rise time was set at 0.2 milliseconds. This feature of the logarithmic amplifier also serves as a filter, ignoring pulses of much longer or shorter duration.

A Tracer-Northern model 1206 multi-channel analyser divided 0-8 volt input into 512 equal channels to store the resistive pulse voltage peaks according to their magnitudes; thereby, providing a frequency distribution of particle number versus channel number. A photograph of the electronic assembly is shown in Figure 5.

Therefore, a relationship between channel numbers and particle diameters can be obtained as follows:

The original signal appearing accross the orifice (ΔVpulse) is given by equation (9). This is amplified by the preamplifier to:

$$\Delta V_{PA} = G \bullet \Delta V_{pulse} \tag{11}$$

with a gain of G=1000, which is then fed to the logarithmic amplifier, whose output is:

$$\Delta V_{LA} = 10/3 \bullet \{\log_{10}(\Delta V_{PA})+2\} \tag{12}$$

and finally appears as a count in a channel number given by:

$$\text{Ch. No.} = 512/8 \bullet \Delta V_{LA} \tag{13}$$

Backprocessing these equations and then numerically solving equation (9), gives a particle diameter range for each channel.

Usually a detailed, 512 channel particle size distribution was not warranted, so the data was recorded as integral number of particles greater than a certain size in steps of 5 or 10 microns. Alternatively, the MCA display could be stored on magnetic tape for future retrieval.

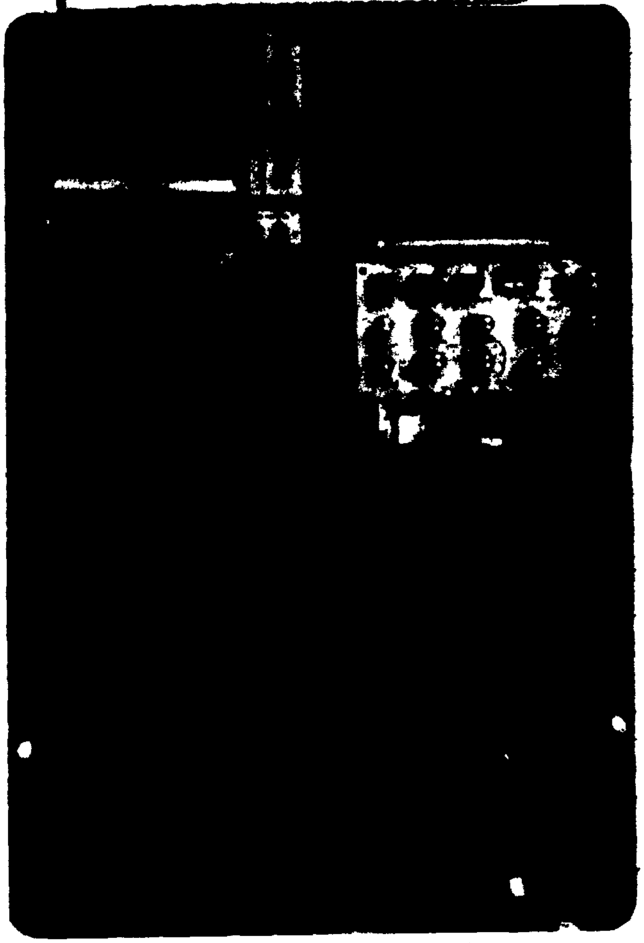

Figure 5 Electronic assembly for pulse detection and measurement. Instrument on top left is the pre-amplifier/oscilloscope, on bottom is the logarithmic amplifier / peak detector and on top right is the multi-channel analyser.

5. DEVELOPEMENT OF THE SYSTEM

To build a system that works for steel, ie. a system that produces noise-free resistive pulse signals, substantial material and design problems had to be overcome. Developement of the electrodes, the sampling cell and the sensing zone are described in the following sections.

5.1. Development of Electrodes

Electrodes serve a dual purpose in the sense that they carry both the heavy DC current and the resistive pulse signals. Requirements for the electrodes were:

i. noise free electrical contacts for sufficiently long duration,

ii. low electrical resistance.

Low electrical resistance was necessary, not only to be able to pass high currents, but also to enable the detection of small pulses riding on a large DC component which is mathematically analogus to taking the difference between two large numbers. From equation (9), the resistive voltage pulses would be modified by a ratio equal to one minus the fraction of circuit potential appearing accross the signal detecting electrodes. In order to minimise this effect and also in order not to exceed the common mode rejection ratio of the pre-amplifier, it was desirable to have as low a DC component as possible. For a maximum total potential drop of one volt across the electrodes for instance, with a 6-V battery as current supply, the total electrode resistance should be less than 1/6th of the total circuit resistance which, for operation at 20 amperes, would be 50 milli-ohms. Alternatively, two extra electrodes could have been inserted for signal detection so as to by-pass the current carrying electrodes and serve as potential measuring electrodes. However, it was felt this would make the system too bulky and difficult to troubleshoot, should one of the four electrodes fail.

Those materials that were tested as electrodes during the course of the present investigation are shown in Table 3, together with typical dimensions and average calculated resistances. In the table, steel electrodes were used in cast iron, as well as others both in cast iron and steel. Cermotherm is a molybdenum, 40% zirconia cermet that has a high resistance to dissolution by molten steel. The metal electrodes met the requirement for low resistance; however, apart from their expense, their performance proved to be unpredictable. When potential drops across the electrodes were monitored with a strip chart recorder during experimental runs in cast iron, metal electrodes sometimes showed unstable and erratic behaviour after 2-5 minutes of immersion. This was probably due to their susceptibility to compound formation. In one particular experiment for instance, when 1% sulphur was added to create MnS inclusions in situ in cast iron, molybdenum electrodes failed to

Table 3
Resistances of Electrode Materials (69,70)

	Resistivity		Dimensions	Average
	20°C	1500°C	Dia. x L	Resistance
	µΩ.m		mm	mΩ
Steel	0.10	1.2	4.8 x 300	11
Molybdenum	0.06	0.46	4.8 300	4
			2.4 300	20
Cermotherm	0.18	1.5	4.8 300	14
Tungsten	0.05	0.5	4.8 300	5
Graphite	10	10	4.8 300	166
			9.5 300	42
			12.5 300	24

Table 4
Thermal Expansion of Shielding Materials (71)

	Thermal Expansion, 20-1500°C
Quartz	0.08 %
Mullite	0.8
Alumina	1.2

conduct. Later, sulphur containing compounds were identified by the scanning electron microscopy at the tips of the failed electrodes. These effects were less of a problem in molten steel.

Graphite electrodes in general performed well but were too bulky for low resistances needed. A combination electrode was therefore developed with graphite ends and molybdenum extensions. Good electrical contact at the threaded connection was established by depositing a small amount of tin between the threads. This arrangement also gave a low cost electrode system where only graphite ends had to be replaced after each experiment.

The electrodes needed to be protected at their sides by a refractory shielding material so as to prevent their dissolving too fast in molten steel. Among the shielding refractories that were tested and are noted in Table 4, quartz had a tendency to soften and chemically reduce in steel. This led to the formation of an insulating intermetallic/complex oxide film coating on the electrode tip with analysed iron contents of 10-20%, Figure 6.

Mullite and alumina both proved to be satisfactory shields, the mullite having more thermal shock resistance, but the alumina being chemically more stable once inserted in the bath without disentegration. Mullite was subsequently preferred because thermal shock resistance was considered to be more desirable. As for chemical stability, Figure 7 shows a graphite electrode inside a mullite sheath after 30 minutes in steel at 1600°C.

COLOURED PICTURES
Images en couleur

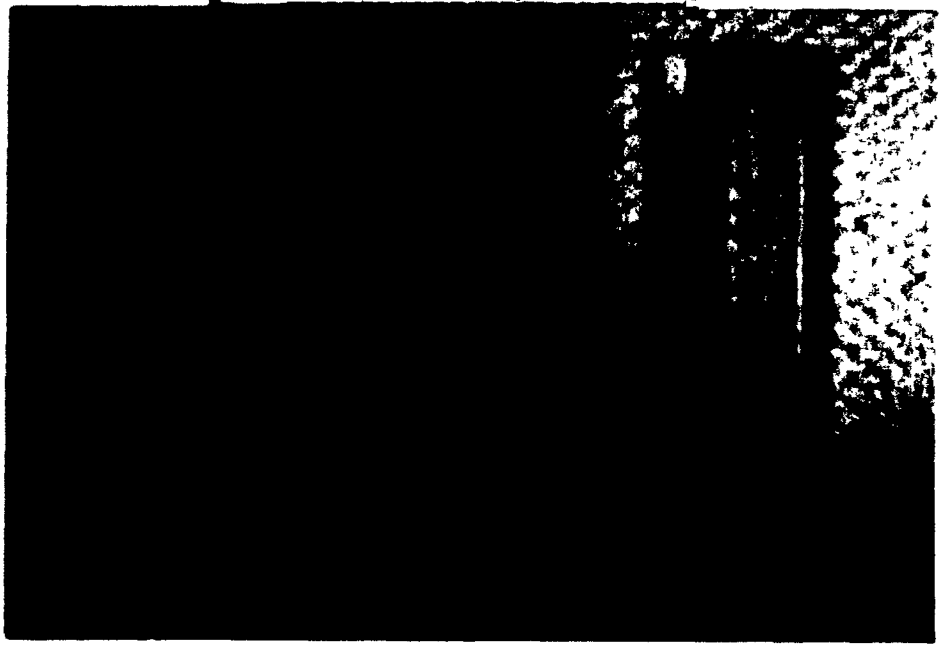

Figure 6 Graphite electrode shielded with quartz, after a steel experiment. The electrode came out intact with a metal globule at the bottom, the area between the concave tip of graphite and the metal globule was smooth and polished and part of it near the edges was covered with a thin film of silica. The outside of silica shield and the metal globule was speckled with intermetallic complex oxide compounds.

COLOURED PICTURES
Images en couleur

Figure 7 Graphite electrode shielded with mullite, after 30 minutes in steel. Initially graphite was exposed 5 mm out of the shield and after the experiment erosion was 20 mm into the shield. Erosion of refractory was high at the slag/metal interface and part of it was completely gone during the course of the experiment to expose some graphite.

Electrode erosion was 20 mm into the shield and the mullite insulation was only partially eroded at the slag/metal interface.

Electrode loss by dissolution did not follow a regular pattern as might be expressed by length of erosion versus time of immersion, but rather depended on whether density driven natural convection currents were set up or not, within the protective shields Those electrodes retaining their initially flat interfaces dissolved much less than those acquiring a needle shaped profile.

Electrodes were tested by inserting a pair into steel/cast iron baths, passing a current, and observing the oscilloscope trace of the pre-amplifier. Almost all electrodes initially displayed noise in cast iron, presumably because of imperfect wetting at the points of contact (see Figure 8). This could be alleviated by passing a heavy current of 200 amps, or by raising the bath temperature to above 1500°C, when a steady baseline would appear on the oscilloscope.

COLOURED PICTURES
Images en couleur

(A)

(B)

Figure 8 Initial electrode noise in cast iron (A), return of a steady baseline after conditioning (B).
Time scale is 1 ms per major division
Vertical Displacement is 50 μV per major division

5.2. Development of Sampling Cell and Sensing Zone

The requirements envisaged for the sampling cell or the sampling tube were:

i. resistance to thermal shock,

ii. resistance to wear at slag/metal interface,

iii. electrical insulation.

It was thought that the electrical sensing zone, or orifice could either be drilled into an insert and the latter attached to the sampling tube or that the orifice might be directly drilled into the side of a sampling tube. Important requirements for the sensing zone were:

i. dimensional stability of the aperture

ii. a smooth entrance for the passage of molten metal.

Quartz and mullite sampling tubes were initially tried because they were readily available and relatively less expensive. The following is an account of some of the attempts carried out to develop a working probe for steel:

A countersunk orifice for smooth entrance to molten metal was drilled onto the side of a mullite sampling tube and for protection against wear, the orifice was plasma sprayed with a zirconia coat. When inserted into steel at 1600°C however, the orifice expanded from 500 microns to 1 mm in one aspiration (see Figure 9).

Quartz sampling tubes with boron nitride inserts at one end containing the orifice along the central axis of the tube were tested in cast iron and other lower melting temperature steel alloys at 1200-1400°C (Figure 10). At these temperatures, the quartz maintained its form; however, difficulty was observed in obtaining noise-free resistive pulse signals especially during aspiration. Subsequent experiments with zinc showed that the location of the orifice along the central axis of the tube was not helpful, possibly because of the turbulance created at the electrode tip by the jetting stream of metal.

When tested in steel, 1 mm thick quartz tubes were not mechanically strong and collapsed above about 1500°C during aspiration (Figure 11).

Figure 12, shows the final arrangement for the resistive pulse probe used for sampling steel melts. A 15 cm long BN tube with a quartz tube extension was used as the sampling cell with the orifice drilled into a BN insert with 82° countersinks on either side. An alumina base cement was used to fix the various components and to provide gas tight seals.

COLOURED PICTURES
Images en couleur

Figure 9 40 mm OD mullite tube with a countersank and zirconia coated orifice after a steel experiment. Orifice expanded from 500 microns to 1 mm in one aspiration.

COLOURED PICTURES
Images en couleur

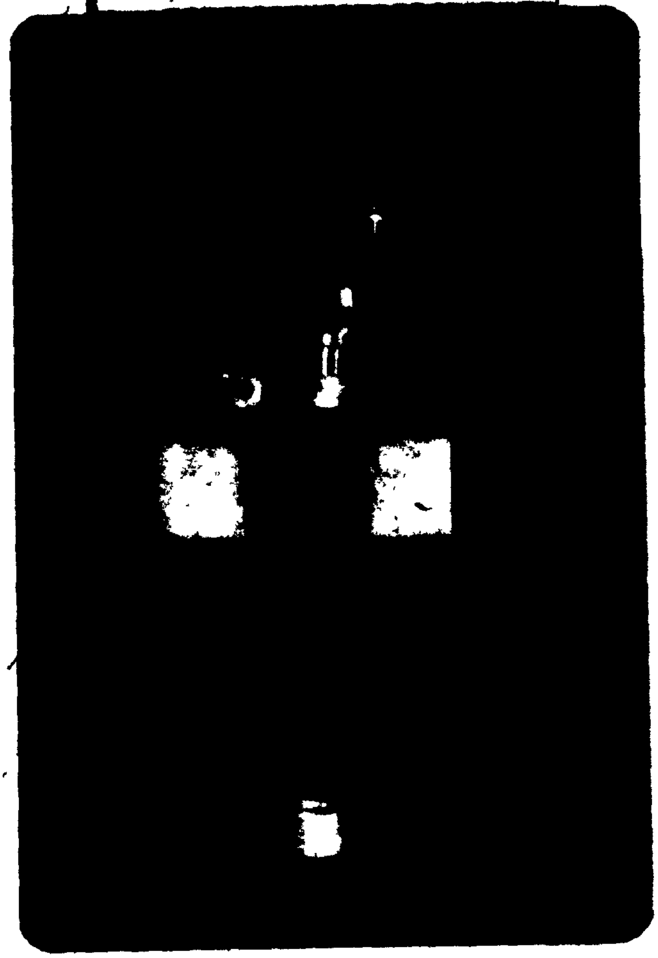

Figure 10 40 mm OD quartz sampling tube with a BN insert carrying the orifice at the bottom, and molybdenum electrodes inside mullite shields

COLOURED PICTURES
Images en couleur

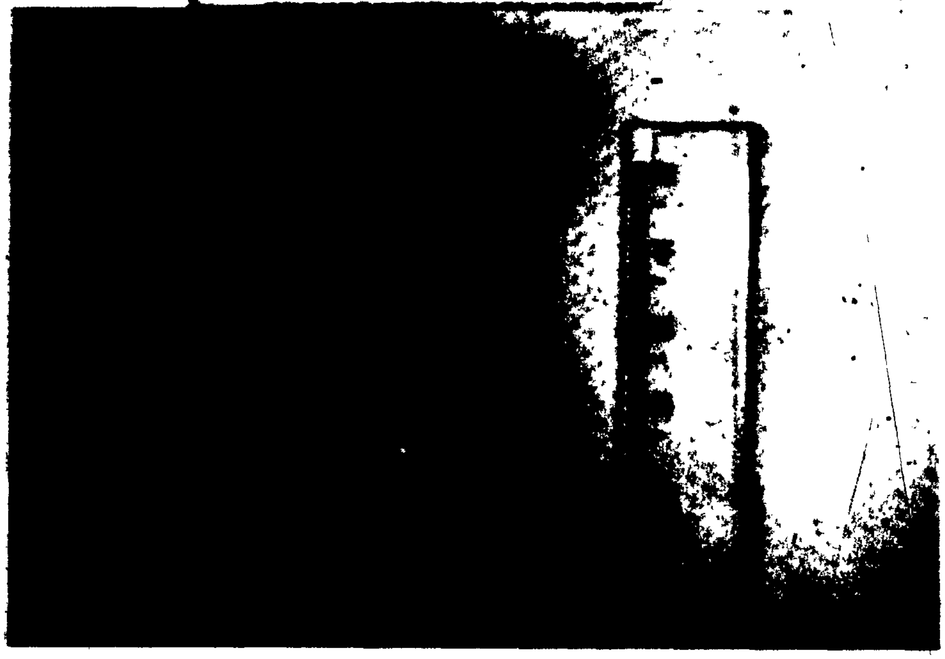

Figure 11 Quartz tube in steel at 1580°C, tube collapsed during aspiration at a differential pressure of 10 cm Hg

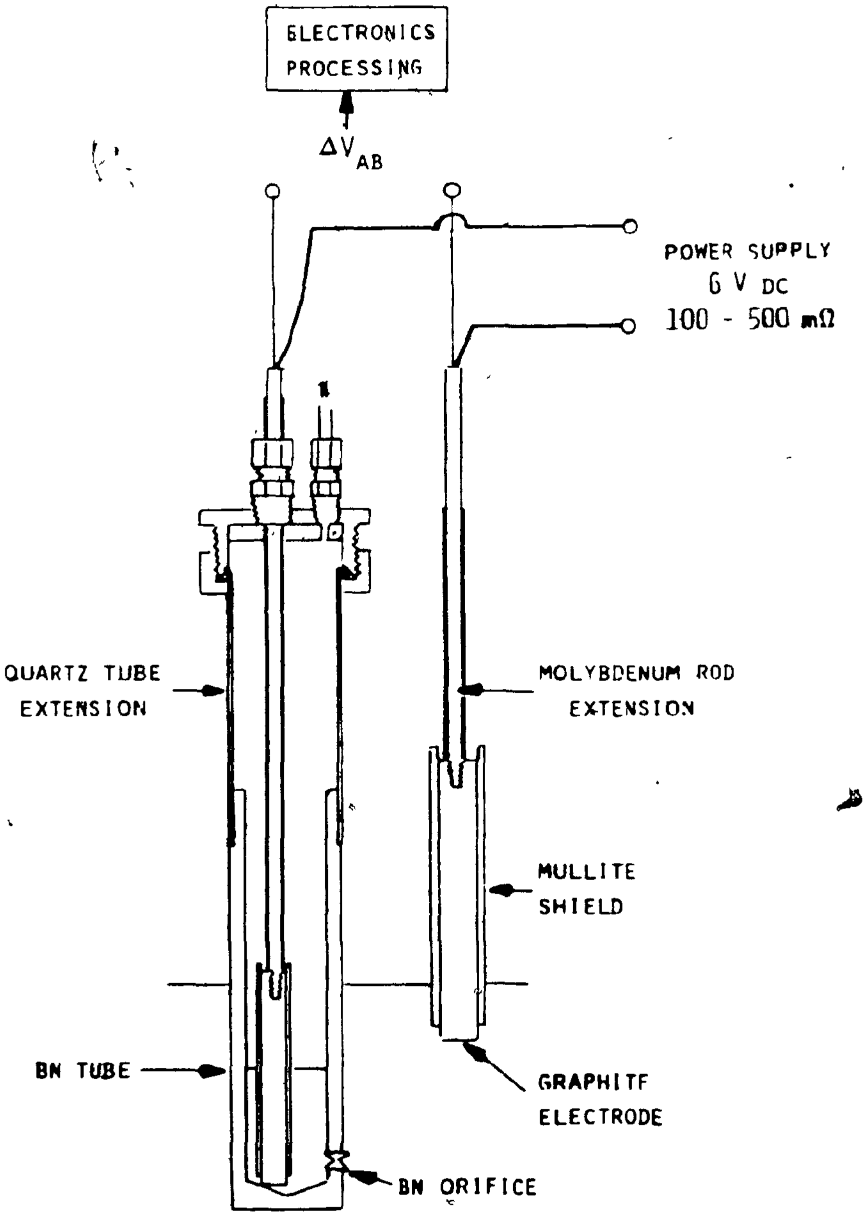

Figure 12 Final Design for the resistive pulse probe for steel.

5.3. System "Troubleshooting"

When testing the system, from time to time unsteady or complete loss of current occurred. To locate the problem, one of the electrodes would be by-passed with a graphite rod inserted into the bath to see if the other was still conducting.

When testing the complete assembly only the outside electrode could be directly checked in this way. If the outside electrode was still conducting, then the problem could be attributed either to orifice blockage or failure of the inside electrode. The inside electrode usually failed because of seperation of the electrode/molten iron interface during aspiration. If repressurising the system did not induce the current to flow again, then orifice blockage would be suspected. Such blockages were also indicated by a slight drop in the gas flowrate.

6. EXPERIMENTAL

6.1. Experiments with Silicon-Boron Steels

The first successful results were obtained in a 3% Si, 5% B steel whose melting point was within 1100-1200°C. This is a high magnetic permeability, low coercivity, commercial alloy used for the transformer and electric motor laminations. This particular alloy is continuously cast into thin sheets of 50 microns thick and cooled suddenly so as to form a glassy, non-crytalline structure which completely eliminates all domain boundaries, hence giving its improved magnetic properties. Measuring the number of inclusions greater than about 10 microns was of interest in order to improve the processing of this material.

6.1.1. Initial Experiments

The alloys were made up using Armco iron, Fe-75%Si, low C ferrosilicon, and Fe-20%B ferroboron, under a protective argon atmosphere in a 60 kg capacity induction furnace. A complete BN tube with a 300 micron orifice located at the bottom, along its central axis was used to sample the steel. An electric current of 50 amperes was passed between inner and outer molybdenum electrodes (Figure 13).

COLOURED PICTURES
Images en couleur

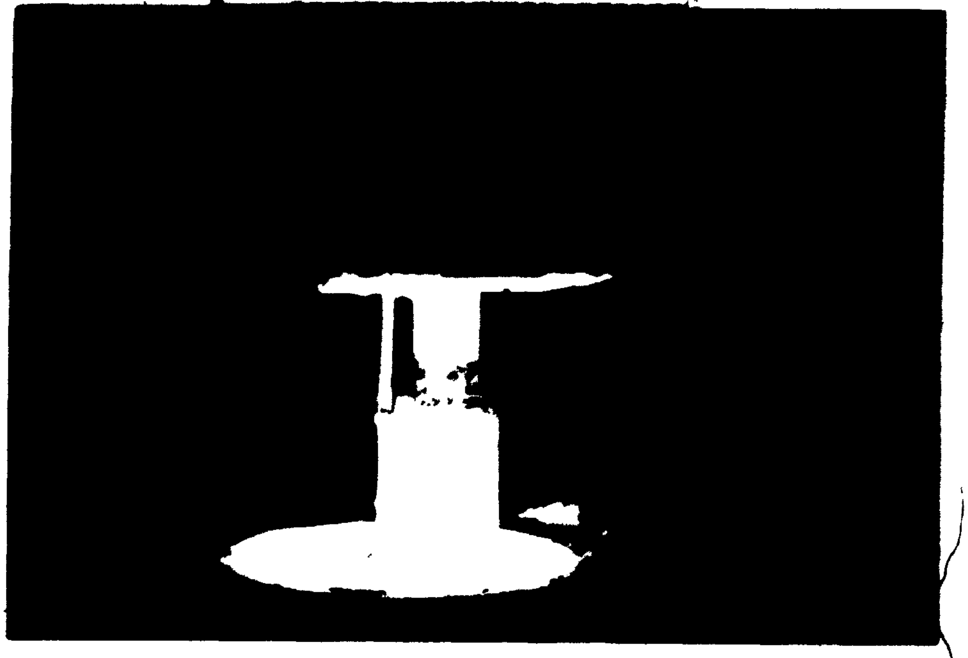

Figure 13 Complete Boron Nitride tube used in the first silicon boron steel experiment, with a 300 micron orifice located at the bottom. The tube was protected with a castable refractory but this was abandonned in later experiments.

During the course of these particle detection experiments, the bath temperature was taken up to 1400°C after which inductive power to the furnace would be turned off prior to sampling. The 60 kg steel would cool to 1200°C in a matter of 5-6 minutes, at which time heating would be resumed again.

In the first two experiments, even after much conditioning with a high current, a steady baseline could not be achieved during aspiration; however, a train of resistive pulses were observed when the tube was being emptied. Figure 14 shows a typical resistive pulse trace that belongs to a ca. 23 micron particle. The thickness of the baseline on the oscilloscope trace is a measure of the electronic noise in the system, which is well below 10 microvolts. The associated 10 second counts of the multi channel analyser which corresponds to an estimated 7.5 grams of steel sample are shown in Figure 15. The MCA image is brightly illuminated from channel 60 onwards, approximately the first major division along the horizontal axis of which corresponds to the selected detection limit of 20 microvolts, or for the above experimental conditions, an inclusion size of ca. 12 microns. The top right corner of the display gives the integral number of counts above this channel number.

The count rates from these experiments were high and contained some 40 micron particles, unexpected for a steel believed to be highly clean. When the probe was subsequently examined, it was found that the area between the shield and the electrode was not completely leak proof and air was able to

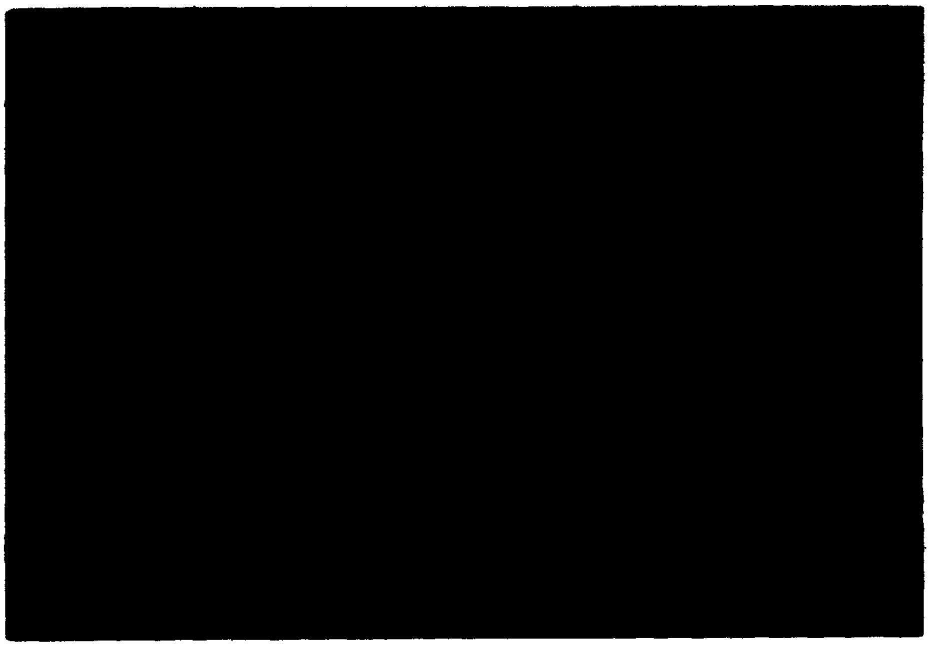

Figure 14 A typical resistive pulse signal obtained while aspirating silicon boron steel through a 300 micron orifice and passing a current of 50 amperes
Time scale is 1 ms per major division
Vertical displacement is 50 μV per major division

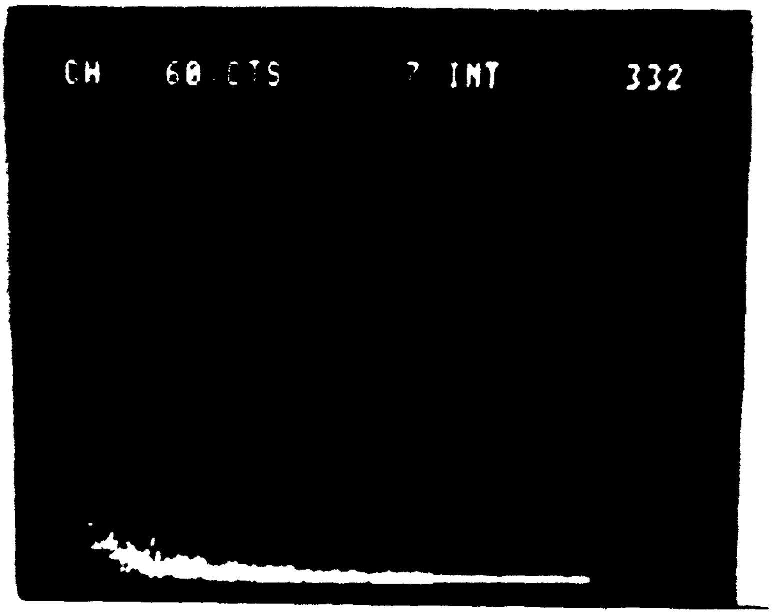

Figure 15 The associated 10 second counts on the MCA corresponding to a calculated 8 gram steel sample. Channel 60 appears at the first major division on the horizontal axis and corresponds to a 20 μV peak or a calculated 12 micron inclusion size.

penetrate via a thin annular slit between the inside electrode and its ceramic protective tube. This absorbtion of air into the chamber took place when the system was on aspiration. The air would then bubble into the steel around the tip of the inside electrode, oxidising it and creating extra borosilicate inclusions. This also partly explains the reason for not having observed a steady baseline during aspiration.

For later experiments, the inside electrode shield was cut into two pieces somewhere below the compression fitting, so as to prevent air reaching the tip.

In later experiments, with the current set at 20 amperes, a steady baseline was generally observed with very few peaks to mark the presence of inclusions. The total number for 10 second counts varied between 0 and 5 particles as shown in Figure 16. The baseline was still somewhat unsteady during aspiration, although not as much as in the earlier experiments. Later experiments with zinc showed that location of the orifice at the bottom, along the central axis of the tube needed improving. A new design, similar to that shown in Figure 9 was therefore adapted.

Figure 17 shows the microstructure of this particular steel under 400x and 1000x magnification, where most inclusions are indeed within 10 microns or less. Figure 18 shows the microstructure after etching in 2% nital to bring up the matrix phases. Inclusions are still visible in the background.

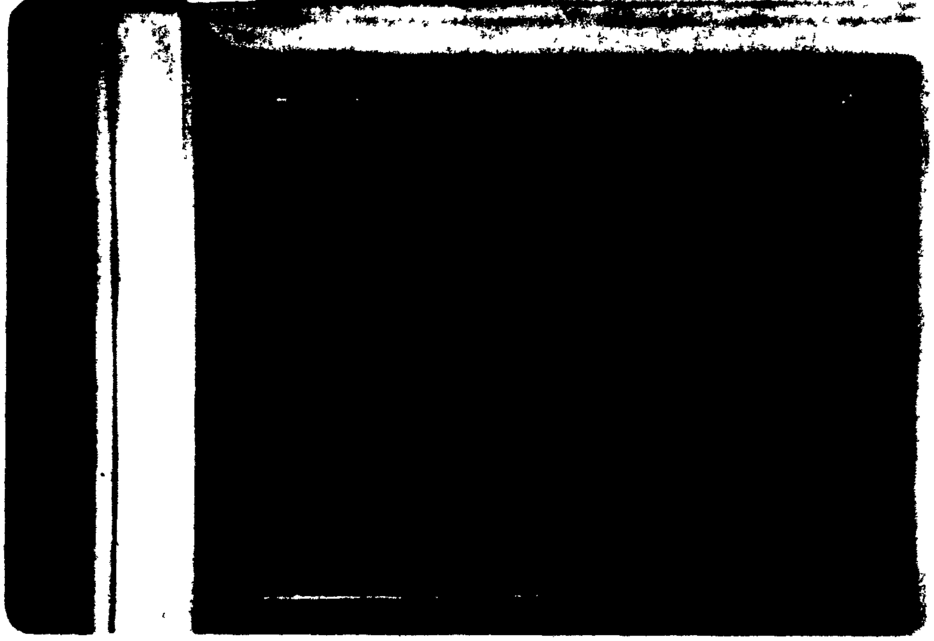

Figure 16 10 second counts on the MCA with the modified probe, calculated 8 gram steel sample. Only 3 counts above channel 60 corresponding to a calculated 17 micron inclusion size are visible.

(A)

(B)

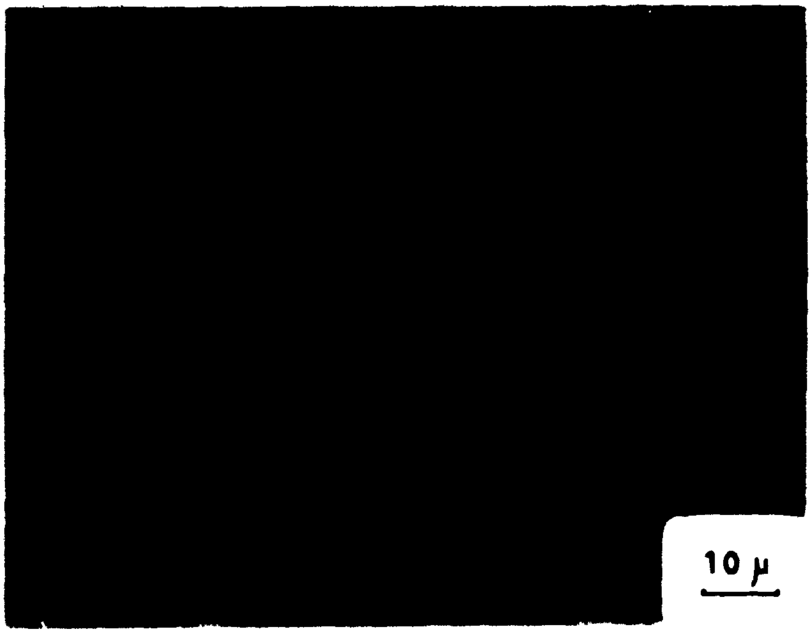

Figure 17 Microstructure of the 3% Si, 5% B steel showing the globular borosilicate inclusions.
Magnification: (A) 400x, (B) 1000x

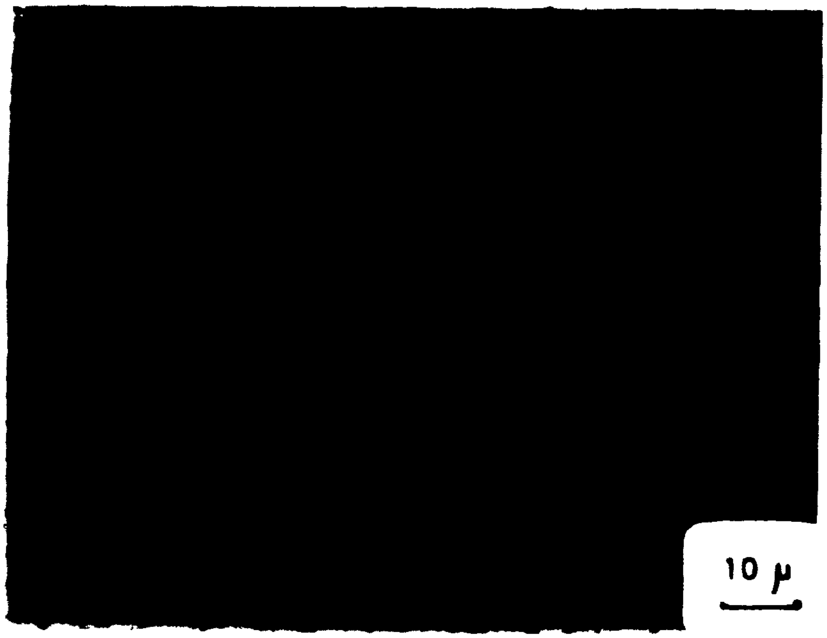

Figure 18 Microstructure of the same steel after etching in 2% nital. Glassy borosilicate inclusions are still visible at the background as one in the middle and anothe lower left hand corner.
Magnification: 1000x

6.1.2. Comparative Experiments in Clean and Contaminated Baths

In order to make a comparative study using the same steel, an attempt was made to disperse a known amount of barium oxide with an average particle size of 50-100 microns as measured under the microscope. Barium oxide has a relatively high density, 5700 kg/m^3, but difficulty was observed in its dispersion because of the slow wetting process by the steel. The mass of barium oxide powder wrapped in an aluminum foil would rather coagulate and float up than be dispersed, even when mixed with powdered ferrosilicon in a ratio one to five.

It was than decided to create particles in situ by additions of 2% Mn, and 1% S, so as to create MnS or complex sulphide inclusions in a 14 kg bath. This type of inclusion was preferred because of its tendency to remain liquid and hence less likelihood of orifice blockage during sampling. However, after a few minutes of sulpher addition, outside molybdenum electrode failed to conduct and the problem was identified to be the sulpher containing compounds at the tip of the electrode, c.f. Section 3.2.

A simpler way of producing indigeneus oxide particles would be to further deoxidise the steel with aluminum. Experiments were therefore planned to take samples before, and after, additions of 0.2-0.02% aluminum. However, in the first experiment, after 0.2% aluminum addition, the current became unsteady and eventually reduced to zero. This was both due to a failed outside electrode and a blocked orifice. When the probe was taken out, it was found to have been covered with a white powder (Figure 19). The same powdery accumulation also appeared around the crucible walls after the metal was teemed out (Figure 20). Subsequent chemical analysis showed it to be pure alumina. This experiment effectively demonstrated the tendency of alumina to attach to free surfaces.

For the next experiment, a larger orifice of 400 microns was used, so as to avoid the problem of blockage, and the probe was inserted 10-15 minutes after a 0.1% Al addition, so as to allow the excess alumina to seperate from the melt. On aspiration, and after a brief conditioning period using high current, a steady baseline and a number of resistive pulse peaks were visible. Figure 21 shows two peaks, one of which is unusual and distorted possibly because of an off-axis particle trajectory, particularly as its residence time was longer than the regular peak.

Associated 10 second counts, i.e. an estimated 13.2 grams of steel sample, showed an average of 150 particles above a detection limit of 24 microns; including some large inclusions of 70 microns, (Figure 22). The orifice aperture did not expand in this particular experiment, it was still 400±5 microns within the accuracy of measurements (Figure 23). The steel's microstructure after the aluminum addition consisted of irregular, and relatively large, alumina inclusions, along with some borosilicates (Figure 24).

COLOURED PICTURES
Images en couleur

Figures 19 and 20 Scale found around the probe, electrode and the inner crucible wall after aluminum addition to the 3% Si, 5% B steel. Chemical analysis of the scale showed only the presence of alumina

COLOURED PICTURES
Images en couleur

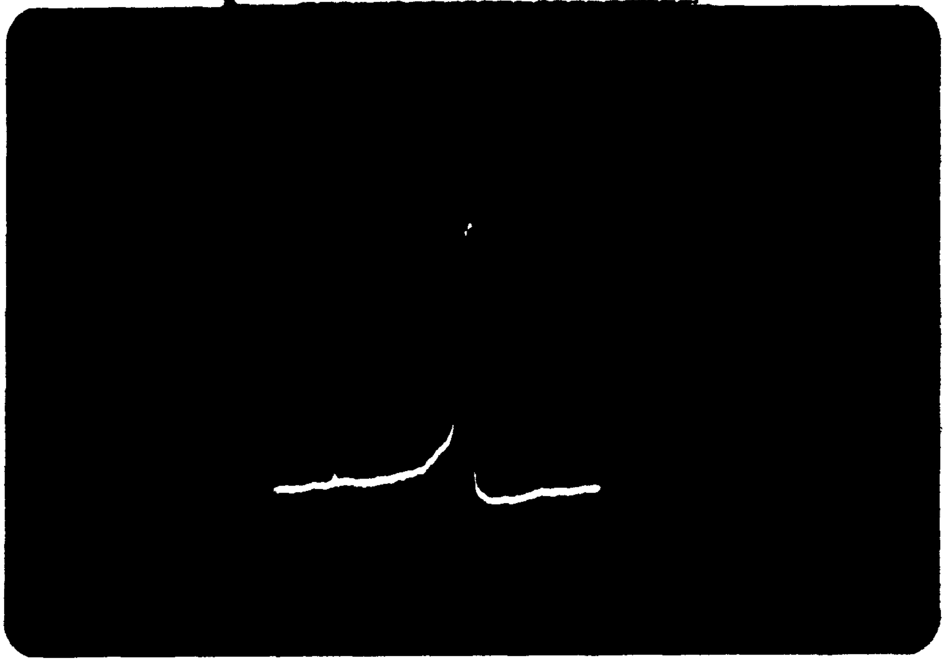

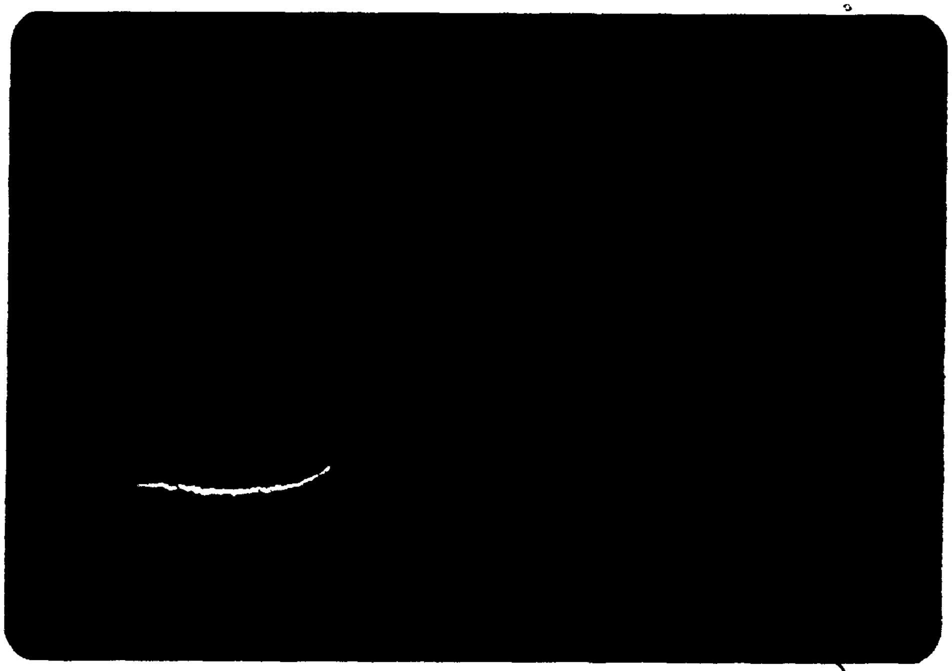

Figure 21 Resistive pulse signals in silicon boron steel after aluminum addition, sampling under 20 amperes with a 400 micron orifice.
Time scale is 1 ms per major division
Vertical displacement is 50 μV per major division

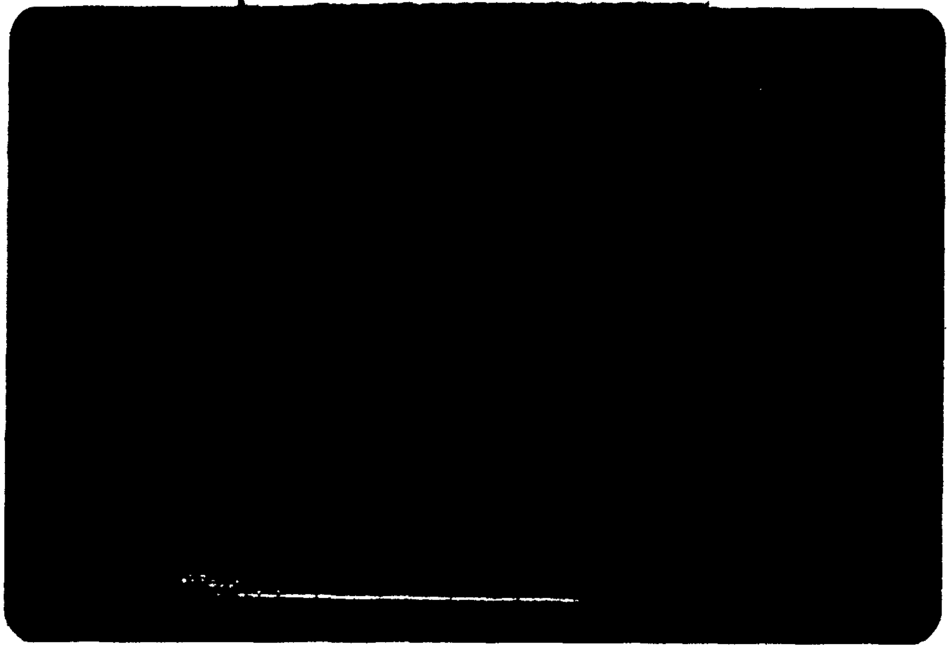

Figure 22 Associated 10 second counts on the MCA after aluminum addition, calculated 13 gram steel sample. Channel 60 (first major division on the left) corresponds to a calculated 26.5 micron inclusion size.

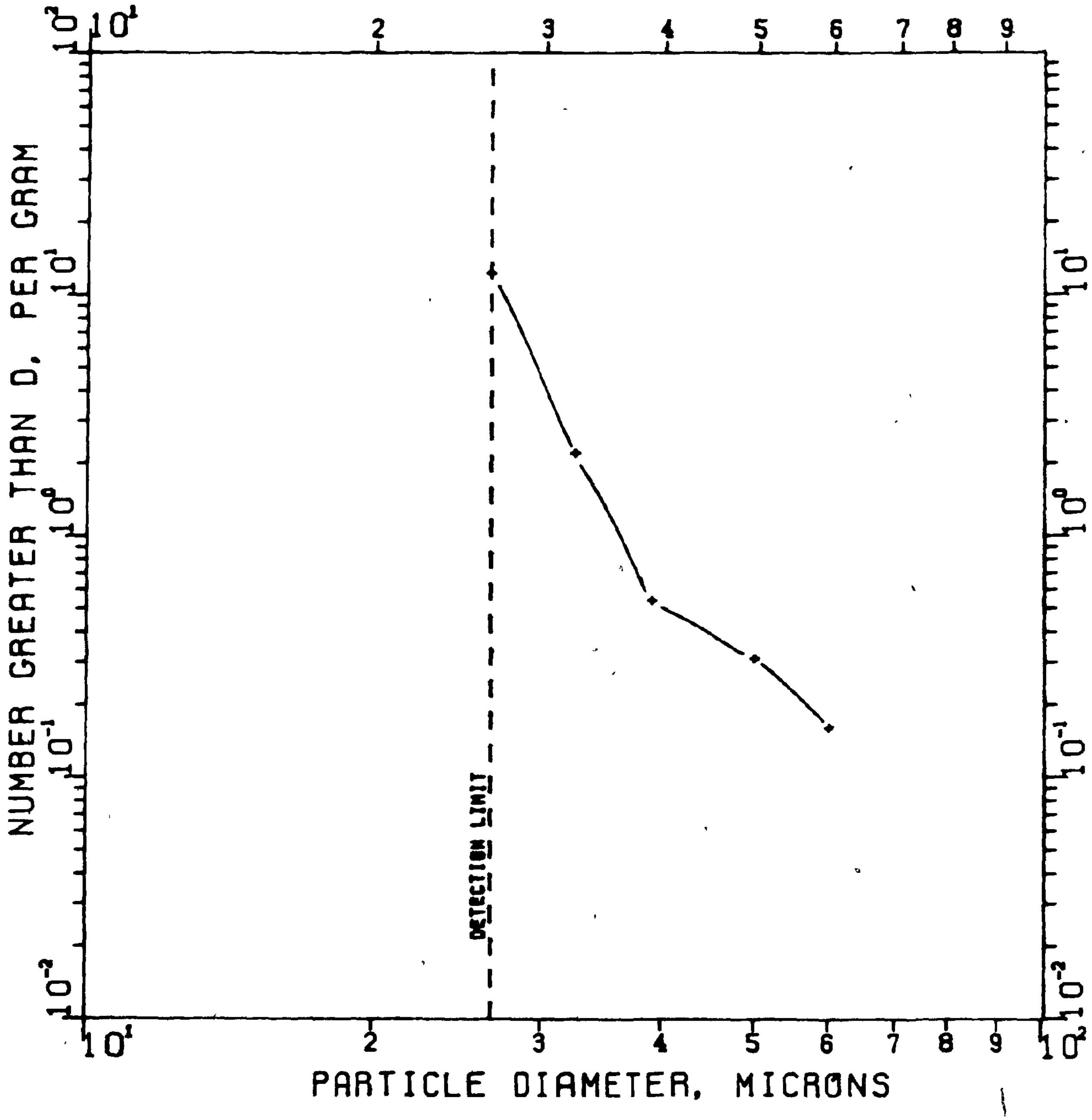

Figure 22-A Size distribution of inclusions in a silicon boron steel after 0.1% Al addition. Calculation is based on the MCA image in Figure 22 and conversion from resistive pulses in microvolts to particle size in microns is made via Figure 3-A.

COLOURED PICTURES
Images en couleur

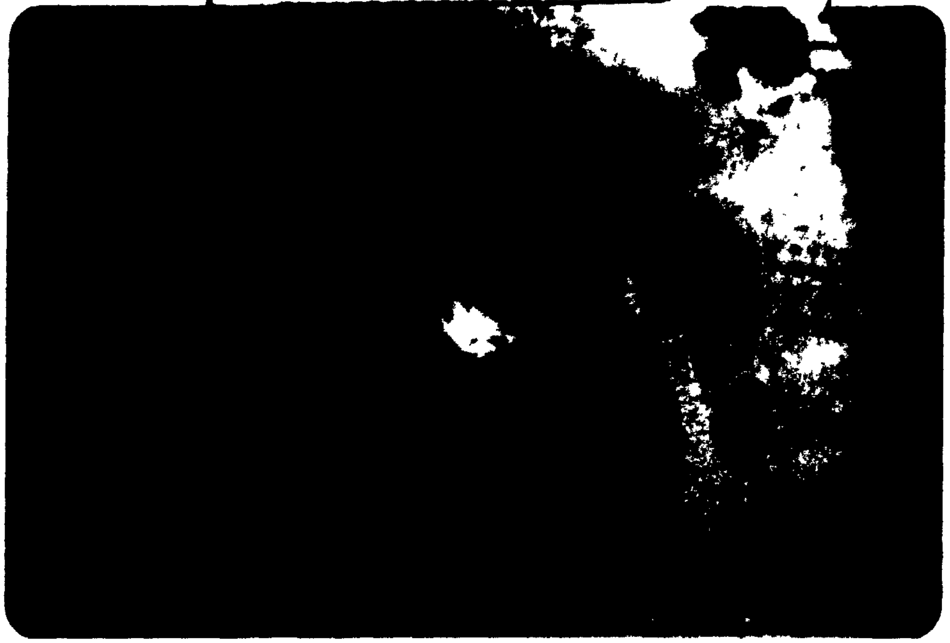

Figure 23 Orifice stability after the silicon boron experiment with aluminum addition. The measured diameters before and after the experiment were 400±5 microns. The diameter of the insert on which the orifice was placed is 6.4 mm (1/4 inches).

(A)

(B)

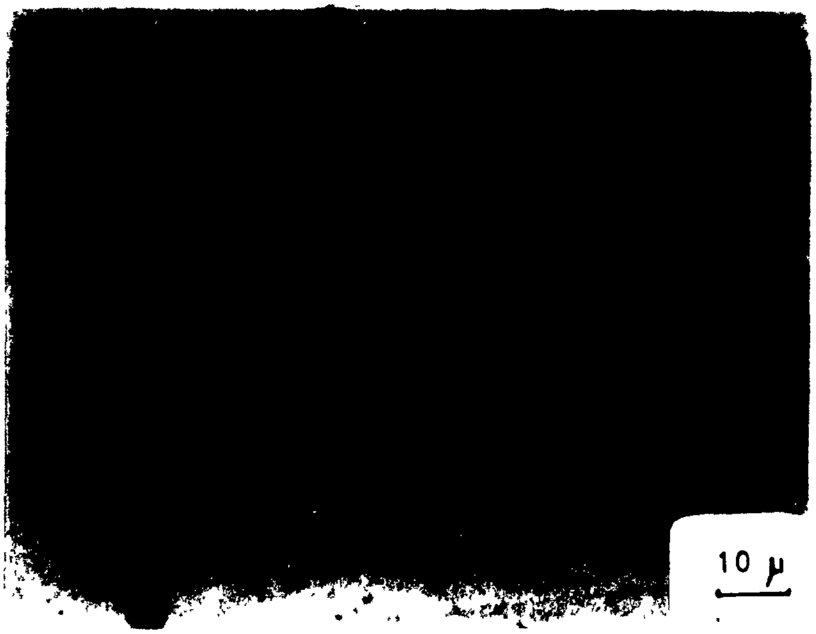

Figure 24 Microstructure of 3% Si, 5% B steel after 0.1% Al addition
Magnification: (A) 400x, (B) 1000x

6.2. Attempts to Identify the Difficulties with Molten Cast Iron and low Carbon Steels

Although parallel experiments had been carried out in cast iron and low carbon steels, attempts to obtain steady baseline voltages on the oscilloscope for these proved to be very difficult. Usually upward spikes, or at best an oscillating baseline such as those shown in Figure 25 were observed. Unfortunately, the period of these oscillations (approximately 1 millisecond) was very close to the particle residence time at the orifice, hence making any electronic filtering action virtually impossible. Experiments were then scheduled using mercury as the fluid medium so as to investigate the effect of variables such as flowrate, and orifice shape, on the onset of baseline instability.

6.2.1. Effect of Flowrate and Orifice Shape on Baseline Voltage Instability

These experiments demonstrated that baseline oscillations would also be encountered in mercury once a critical metal flowrate was reached. These oscillations occurred initially as ripples, and then grew into larger oscillations of the type shown in Figure 26, as the mercury flowrate was further increased.

(A)

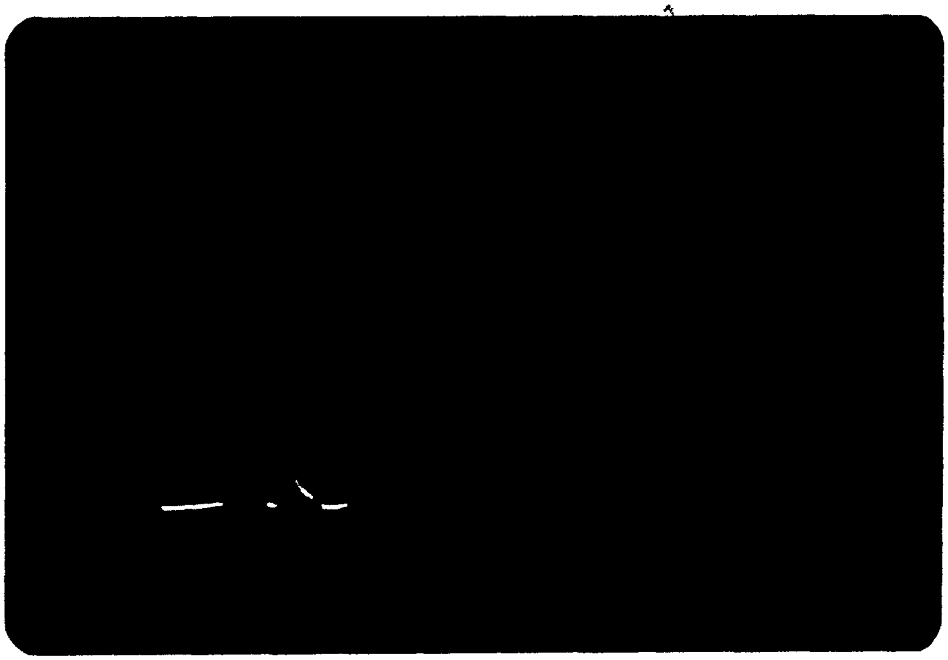

COLOURED PICTURES
Images en couleur

(B)

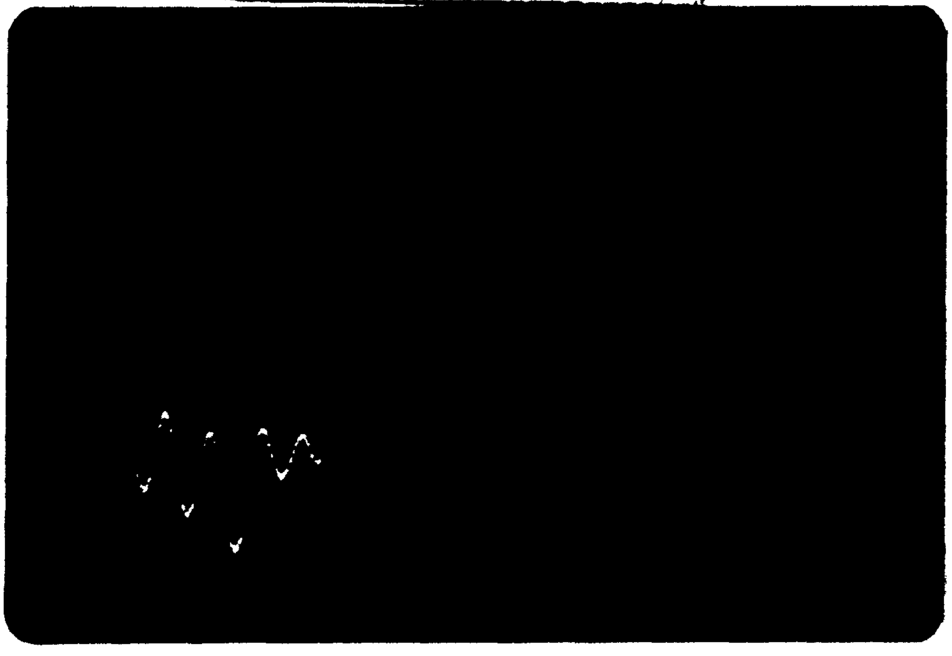

Figure 25 Unstable baselines, (A) upward spikes usually associated with unsteady current, (B) oscillating baseline

COLOURED PICTURES
Images en couleur

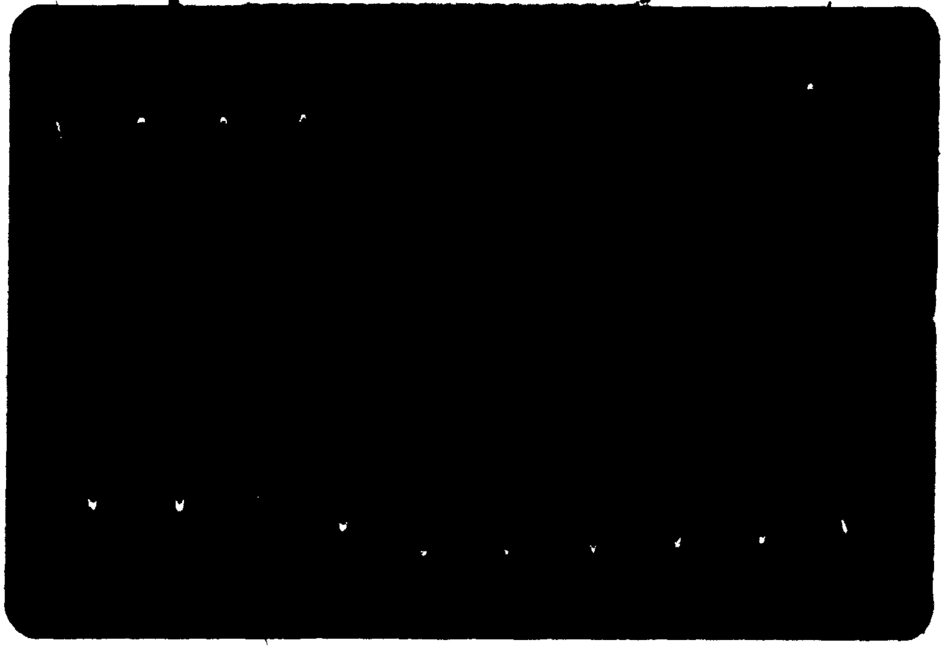

Figure 26 Baseline oscillation in mercury associated with high flow rate.
Time scale is 1 ms per major division
Vertical displacement is 50μV per major division

Two types of orifices were tested: i) BN orifices of different diameters and 0.5 and 1 mm long, drilled into a BN insert with 82° countersinks on either side, ii) the 300 micron Alcan orifice as used in the LiMCA equipment for sampling aluminum, a cross-section of which is shown in Figure 27.

The results of these experiments can be summarised as follows:

1. Baseline instability started at a repeatable suction pressure corresponding to a critical velocity.

2. Smaller orifices tolerated higher suction pressures.

3. Orifices with smooth entry tolerated much higher suction pressures.

4. Oscillations disappeared once the current current was turned off, yielding to a steady baseline voltage.

5. Similar transitions were also observed using an equivalent water-based probe.

Table 5 gives some quantitative data in which average metal velocity and the Reynold's numbers have been estimated from the corresponding critical suction pressures. For the BN type orifice, the existence of a critical Reynold's number suggests that some form of inertia driven fluid movement, perhaps the

Figure 27 Cross-section of a 300 micron orifice, flame drilled and polished into the side of a Kimax culture tube as used in LiMCA measurements in Alcan

Table 5
Critical Suction Pressures and Corresponding Calculated Average Metal Velocities At Which Baseline Oscillations Start in Mecury.

Orifice Type	Orifice Diameter	ΔP_{cr}	$\bar{u}_{cr}$	Re_{cr}
	μm	cm Hg	m/s	
(1)	250	16	1.24	2580
	350	8	0.88	2560
	400	7	0.82	2735
(2)	300	>30	>1.71	>4500

(1) BN Orifice with 82° Countersunk Entry, Re_{cr} =2500

(2) Alcan's Glass Orifice with a Fluted Entry, Re_{cr} >4500

Table 6
Relative Susceptibility to High Reynold's Numbers (RSHR) for Some Fluids of Interest

	Hg	Ga	Al	Water	Fe
M.P. (°C)	-39	30	660	20	1535
Density (kg/m³)	13600	6090	2400	1000	7000
Viscosity (mPa.s)	1.56	2.04	1.3	1.0	7.0
R.S.H.R.	2.4	1.2	1.2	1	0.4

formation of a vena-contracta (72) at the orifice entrance is responsible for inducing baseline oscillations. The far superior performance of the Alcan orifice lends support to this hypothesis.

Assuming that for a given orifice shape, baseline instability is caused by a critical Reynold's number, $\bar{u}.D/\nu$ and since $\bar{u} \propto \sqrt{\Delta P/\rho}$), then a fluid property indicating its Susceptibility to High Reynold's numbers may be defined as:

$$SHR = \sqrt{\rho}/\mu \qquad (14)$$

Table 6 shows SHR values for some fluids of interest, on a scale where the value for water is taken as 1. From the table it can be seen that mercury is the most susceptible fluid, steel is the least and aluminium and gallium fall somewhere in between.

The above analysis suggests that for the suction pressures being used, the geometry of the BN orifice should not have been a problem in either cast irons or low carbon steels.

6.2.2. Potential Effects of Melt Composition in Promoting Chemical Reactions in the Hot Zone of the Orifice

The major experimental problem with cast iron lay in the fact that it was not possible to pass a good "conditioning current" through the orifice. At 20 amperes, the current would tend to stay steady, but once the ballast resistor was shorted, the current would briefly climb to some 40-80 amps and then fall back to zero. This would then be repeated at short intervals.

A high current of 100-150 amps passing through a 300 micron orifice is able to cause a rate of temperature rise of several hundred degrees centigrade per millisecond at the orifice. It is presently believed that this 'conditioning current' helps to completely wet the orifice wall and remove any adhering particles, therefore leading to steady baselines (53).

Since the basic difference between silicon-boron steels and cast iron lay in the chemical composition, it was then decided to examine the possibility of a chemical reaction leading to the formation of gaseous products and attendant baseline instabilities.

Formation of silica from dissolved oxygen and silicon in iron has a very large enthalpy term, so that silica particles in molten iron become increasingly unstable at high temperatures. Figure 28 shows the free energy change associated with the reaction:

$$SiO_2 + 2\,\underline{C} = \underline{Si} + 2\,CO_{(gas)} \qquad (15)$$

versus temperature, extrapolated to above 1800°C, for the compositions of cast iron and low carbon steel used in the experiments.

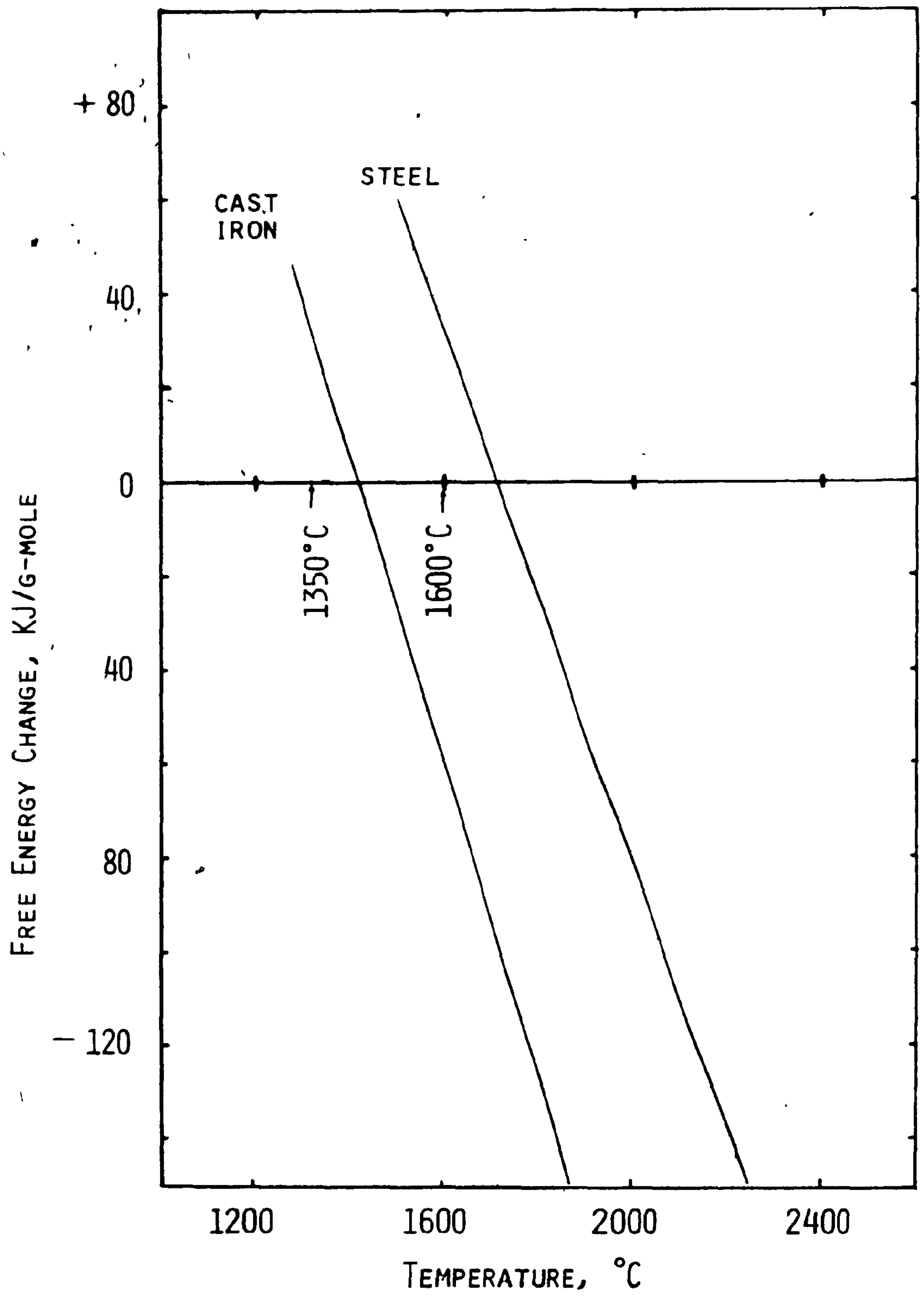

Figure 28 Free energy change associated with the reaction (15).

Figure 28, continued:

Free energy change for the reaction (15) may be evaluated using the data for the following reactions:

$$\underline{C} + \underline{O} = CO_{(gas)} \qquad (16)$$

$$\Delta G^\circ_{(16)} = -17,900-14.19\ T \quad J/g\text{-}mol \ (73)$$

$$\underline{Si} + 2\ \underline{O} = SiO_2 \qquad (17)$$

$$\Delta G^\circ_{(17)} = -594,000+230\ T \quad J/g\text{-}mol \ (74)$$

For reaction (15), using Hess' law:

$$SiO_2 + 2\ \underline{C} = \underline{Si} + 2\ CO_{(gas)} \qquad (15)$$

$$\Delta G^\circ_{(15)} = 2\ \Delta G^\circ_{(16)} - \Delta G^\circ_{(17)}$$

$$= 558,200 - 312.38\ T \quad J/g\text{-}mol$$

where standard state for components dissolved in liquid iron is at infinite dilution, on a weight percent scale. Hence the free energy change for a given initial concentration is:

$$\Delta G_{(15)} = \Delta G^\circ_{(15)} + RT \ln \left[\frac{h_{Si}\ p^2_{CO}}{h^2_C\ a_{SiO2}}\right] \qquad (18)$$

Case 1: Steel initially at 1600°C

Composition: 0.1 C, 0.5 Si, 0.2 Mn, 0.02 S, 0.02 P, ca. 0.0075 O

1. Calculation of the Activity of Silicon

$$h_{Si} = f_{Si} \bullet \% \, Si \qquad (19)$$

using the interaction coefficients in ref. (75):

$$\text{Log } f_{Si} = 0.1[\%Si]+0.2[\%C]+0.2[\%Mn]-0.2[\%O]+0.1[\%P]+0.06[\%S] \qquad (20)$$

$f_{Si} = 1.25$ and $h_{Si} = 0.63$ are found.

2. Calculation of the Activity of Carbon

$$h_C = f_C \bullet \% \, C \qquad (21)$$

again using interaction coefficients (75):

$$\text{Log } f_C = 0.2[\%C]-0.008[\%C]^2+0.1[\%Si]-0.01[\%Mn]+0.1[\%P+\%S]-0.3[\%O] \qquad (22)$$

$f_C = 1.18$ and $h_C = 0.118$ are found.

3. Free Energy Change for Reaction (15) with Temperature: assuming $p_{CO} = 1$ and $a_{SiO_2} = 1$ in equation (18):

$$\Delta G = \Delta G° + RT \ln (h_{Si} / h_C^2)$$

$$= 558{,}200 - 280.69\,T \quad \text{J/g-mol} \tag{23}$$

This line is plotted in Figure 28 for steel.

Case 2: Cast Iron initially at 1350°C

Composition: 4.2 C, 3 Si, 3 Mn, 0.01 S, 0.03 P

1. Calculation of the Activity of Silicon: Again using the interaction coefficients of the previous example, $f_{Si} = 55$ and $h_{Si} = 165$ are found.

2. Calculation of the Activity of Carbon: Since interaction coefficients are applicable only in dilute solutions, a different method proposed by Fuwa and Chipman (76) and presented in ref. (77) may be used to evaluate activity coefficient of carbon in concentrated solutions. The final expression in the integrated form is:

$$\text{Log}\,\frac{f_{c,\text{final}}}{f_{c,\text{binary}}} = -1.21 \sum_{i=1}^{n} \left[\frac{\partial \ln(x_c)}{\partial x_i} \Delta x_i \right] \tag{24}$$

where $\partial\ln(xc)/\partial xi$ is the change in carbon solubility with additions of solute (i) in mole fractions. Using the table in ref. (78):

$$\text{Log}\, f_c = -1.21\{-3.7[\%Si]+0.5[\%Mn]-5.2[\%S]-4.6[\%P]\} +$$

$$0.2[\%C]-0.008[\%C]^2 \quad (25)$$

$f_c = 8.7$ and $h_c = 36.5$ are found. The last two terms in equation (25) give the value of Log ($f_{c,binary}$)

3. Free Energy Change for Reaction (15) with Temperature

$$\Delta G = 558{,}200 - 329.74\ T \quad \text{J/g-mol} \qquad (26)$$

This line is plotted in Figure 28 for cast iron.

Assumptions:

1. Equilibrium constants are used outside their temperature range: 1350-2200°C.

2. Activities h_{si} and h_c are fixed by composition and assumed not to vary with temperature.

3. Effect of transformations such as

$$SiO_{2\,(s)} = SiO_{2\,(l)} \qquad \text{at } 1723°C$$

are neglected.

It is clear from Figure 28 that there will be an excess free energy on the surface of a silica particle for the formation of CO gas. It is not clear however how the reaction would take place, in terms of nucleation and growth, in such a short span of time. One possible mechanism would be the adhesion of sub-microscopic silica particles to the orifice wall, supplying oxygen for CO nucleation, hence cutting the conditioning current prematurely before it has a chance to grow and remove all the adhesed particles.

A similar phenomenon was also observed in the boron-silicon steels, although to a much lesser degree. When the ballast resistor was shorted, the current would gradually build up to 40-80 amps in a stepwise fashion and would then suddenly grow to 150 amps, indicating a clear path through the orifice. The stability of borosilicate particles was perhaps the key factor in the initial success of the "LiMCA" technique with this particular alloy.

6.3. Experiments with Cast Iron

In the light of the preceeding section, the first modification to the BN orifice inserts were made with respect to their lengths. The original aspect ratio of 1 mm long to 0.3 mm diameter orifice was considered to be high; as this might give rise to Rayleigh instability and, during the conditioning stage, to excessive heat at the orifice exit while leaving the area near entry largely unconditioned. The orifice length was therefore reduced to 0.5 mm.

To promote the formation of the more stable manganese silicates, an addition of 3% Mn was also planned. When experiments were performed in a 4.2% C, 2% Si, 3% Mn cast iron with a 300 micron diameter orifice, it was possible to obtain a steady baseline by first passing an initial high current of 200 amperes and then sampling under 20 amperes. Only few resistive pulse peaks as in Figure 29 were observed indicating a clean (i.e. inclusion free) bath. These peaks had shorter residence times because of the shortened orifice length. The expansion of the orifice aperture in these experiments was high, of the order of 20 microns per aspiration. The effect of orifice expansion on the particle size measurement is discussed in Chapter 7.

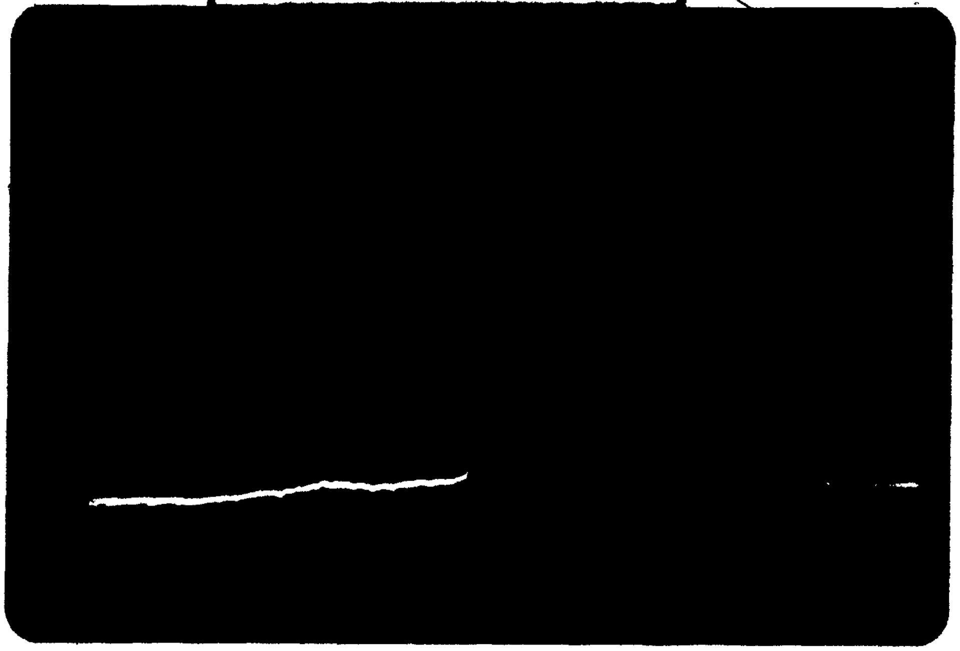

Figure 29 A typical resistive pulse signal obtained while aspirating cast iron through a 300 micron orifice and passing a current of 20 amperes. The 40 μV signal belongs to a 23 micron particle.
Time scale is 1 ms per major division
Vertical displacement is 50 μV per major division

7. SELECTION OF MEASUREMENT CONDITIONS

Initially similar conditions as those for aluminum, i.e. 300 micron orifice diameter, 50 amperes of current, 12.5 cm Hg vacuum pressure and 20 microvolts detection limit were used. These were then modified during the course of experiments. The selection of optimum measurement conditions were made on the basis of the physical principles and the experimental results presented in Chapter 5.

7.1. Selection of Orifice Diameter

It was desirable to select an orifice diameter that would give sufficient resolution to detect inclusions of interest yet not too small as to increase the likelihood of blockage. The choice of orifice diameter depended then on the steel cleanliness expected. As the micrographs of the silicon-boron steel in Figure 16 show, steel deoxidised with Si, Mn, B or their combinations will contain numerous but small inclusions. An orifice as small as 200 microns could therefore be used in this case, with little risk of blockage. Aluminum killed steels on the other hand, tended to contain coarser inclusions (agglomerates), which in conjunction with their tendency to accumulate on free surfaces made blockage of the orifice more likely. For this type of steel therefore, 400-600 microns orifice tended to be more suitable on the basis of present tests.

7.2. Selection of Aspiration Pressure

The minimum vacuum necessary to aspirate the steel by first overcoming surface tension forces at the orifice depends on the orifice diameter. For a completely non-wetting orifice, the gauge vacuum necessary is given by:

$$\Delta P = 4\sigma/D \qquad (27)$$

where σ is the surface tension of the steel. Values of ΔP for orifice diameters ranging from 200-600 microns are listed in Table 7. If the orifice wall is partially wet by steel, then these values should be multiplied by a factor $|\cos\theta|$, where θ is the contact angle. In the actual experiments, after adjusting for ferrostatic pressure, 14 cm Hg (18.7 kPa-g) vacuum was found sufficient for 300 micron orifice giving a contact angle of approximately 140° between boron nitride and steel, taking σ=1.87 N/m (69). Approximately 85% of the values in Table 7 were therefore taken as being a sufficient operating differential pressure. These are presented in Table 9

7.3. Relationship Between Aspiration Pressure and Sampling Rate

To estimate the discharge coefficient (CD) of the orifice and hence metal velocity at the orifice and sample volume taken, experiments were conducted with zinc, which has a similar density to that of steel, by measuring the time taken to fill a given volume under varying differential pressures using a 300 micron

Table 7
Minimum Pressure Required to Force Molten Iron Through a Non-wetting Orifice [σ=1.87 N/m] (69).

Orifice Diameter	Required Pressure Difference	
µm	cm Hg	kPa
200	28.1	37.5
300	18.7	24.9
400	14.0	18.7
500	11.2	15.0
600	9.4	12.5

diameter, 1 mm long BN orifice. Results of these experiments are shown in Table 8, together with computed values of corresponding Reynold's numbers (Re). As seen from inspection of Table 8, CD decreased considerably with decreasing differential pressure, most likely because of the increasing effect of viscous dissipation.

Since viscous dissipation in the laminar regime is a function of Re alone (72), it is safe to assume that for a given orifice, CD should be the same for different fluids at the same Re. More accurate measurements with water with a similar orifice confirmed the almost linear increase in CD with increasing Re over the range 800<Re<2400. At Re=2400-2600, a discontinuity was observed in the water experiments, when the discharge coefficient dropped sharply to a lower value but then again increased, suggesting a change in the flow regime; either as a result of a transition to a turbulent jet at the orifice exit or the formation of a vena-contracta at the entry.

To make an estimate for average metal velocity and 10 second sample volumes in steel experiments, a linear relationship between Re and CD was assumed in the range 400<Re<1000 applicable to both zinc and steel. Such linear relationships between Reynold's number and the entry or exit losses have, in fact, been predicted theoretically and observed experimentally in laminar pipe flow (79). A least square fit was then made to the values of CD, obtained from the zinc experiments. The last column in Table 8 shows the accordingly adjusted values of CD where

Table 8

Estimation of Discharge Coefficient of the 0.3 mm diameter 1 mm long BN orifice from zinc experiments. Last column gives the linear least square fit values of Re vs CD, correlation coefficient r=0.98.

Differential Pressure ΔP	Metal Velocity $\bar{u}_{Zn}$	Re	C_D	$\bar{C}_D$
cm Hg	m/s			
6	1.05	525	0.67	0.66
8	1.20	600	0.66	0.68
10	1.42	710	0.70	0.70
12	1.60	800	0.72	0.72
16	1.98	990	0.77	0.76
20	2.24	1120	0.78	0.79

Table 9
Estimated Values of Discharge Coefficient, Reynold's Number, Average Metal Velocity and 10 s Sample Volume at the Proposed Operating Differential Pressure for Varying Orifice Diameters. Kinematic Viscosity of Iron, ν=0.9 mm2/s (ref62).
1 kPa = 0.75 cm Hg

Orifice Diameter	Differential Pressure, ΔP	Discharge Coefficient	Re	$\bar{u}$	10 second Sample Volume
µm	cm Hg			m/s	grams
200	24	0.64	430	1.93	4.25
300	16	0.66	547	1.64	8.1
400	12	0.69	653	1.47	12.9
500	10	0.71	773	1.39	19.1
600	8	0.73	848	1.27	25.2

correlation coefficient with Re is 0.98. Starting with an initially guessed value for CD, the average metal velocity at the orifice and the 10 second sample volume were then calculated for molten iron as a function of orifice diameter and applied vacuum (Table 9).

Alternatively, a direct measurement of metal velocity at the orifice could be made by measuring the residence time of a particle from the oscilloscope trace, except for the difficulty of estimating the exact time of particle entry to and exit from the orifice.

7.4. Operating Current and Minimum Detectable Inclusion Size

For a given electrode and orifice resistance (R_E), the optimum current to deliver the maximum pulse could be found by differentiating equation (7) with respect to R_B, keeping R_E constant, and equating the derivative to zero. This results in $R_E = R_B$ and $V_E = 3$ volts with a 6 volt battery as the power source. With graphite tipped electrodes, R_E was of the order of 50 mΩ. Using a ballast resistor of similar resistance would yield a circuit current of 60 amperes. Increasing the current beyond this value by reducing the ballast resistance will reverse the effect of current and make the voltage pulses smaller. In fact, the recommended maximum current would be one third of this value because:

i. it is desirable to have as low a DC component across the electrodes as possible; preferably not more than 1 volt,

ii. because of diminishing returns, as can be seen in Table 11-(B), there is no significant gain in detection limit beyond an applied current of 20 amperes which corresponds to $R_B = 5R_E$ for $R_E = 50$ mΩ.

With metal electrodes, or with additional signal detecting electrodes inserted into the bath, much higher currents could of course be used before ballast resistance reaches the above limit of 5xRE.

Another restriction to the current is the possibility of excessive heating at the orifice. In view of the short residence times, 10-40°C/ms was considered to be a moderate rate of temperature rise and, corresponding currents were used for the orifice size at hand. Rate of temperature rise is given by:

$$dT/dt\big|_{t=0} = \rho_e \iota^2 / \rho C_p \qquad (28)$$

where the numerator is the volumetric rate of heat evolved by Ohm's law ($\rho e = 1.4 \times 10^{-3}$ Ω.mm (69)) and the denominator is the volumetric heat capacity of steel, 5.6×10^{-3} J/mm³.°C (80). Calculated temperature rise at the orifice exit for different orifices and currents are shown in Table 10 with tolerable levels underlined.

Table 10
Rates of Temperature Rise at Orifice for Given Applied Currents
Moderate Values are Underlined.

Orifice Diameter	Current, amperes			
	5	10	20	40
µm	Rate of Temperature Rise, °C/ms			
200	6	<u>25</u>	100	400
300		5	<u>20</u>	80
400			6	<u>25</u>
500				10
600				5

Table 11
Minimum Detectable Inclusion Sizes using Different Electrode Arrangemets.

(A) Extra Signal Detecting Electrodes, R_E is Neglected

Orifice Diameter	Current, amperes			
	5	10	20	40
µm	Minimum Detectable Particle Diameter, µm			
200	15	12	10	
300		21	17	13
400		31	24	19
500		41	33	26
600			42	33

(B) Graphite Tipped Electrodes, R_E = 50 mΩ

Orifice Diameter	Current, amperes			
	5	10	20	40
µm	Minimum Detectable Particle Diameter, µm			
200	16	12.6	10	
300		22	18	18
400		32	26.5	26
500		43	36	35
600		55	46	45

In the steel experiments, it has been possible to attain a noise level as low as 5-10 microvolts by proper shielding and by the elimination of magnetic and mechanical disturbances. This enables the selection of 20 microvolts as the pulse detection limit with a signal to noise ratio of 2. Minimum detectable inclusion sizes can than be calculated by use of equation (9) at the recommended operating currents and are given in Table 11. On the same table a comparison is also made to show the effect of electrode resistance on the detection limit, which becomes increasingly important at higher currents. In Table 11-(B), for the purpose of calculating minimum detectable inclusion sizes, the total resistance across the electrodes is obtained by adding a calculated orifice resistance (0.5 mm long) to RE.

7.5. Estimation of the Level of Required Conditioning Current

The net effect of the "conditioning current" is the intense, localised generation of heat at the orifice. For a 300 micron orifice, 200 amperes was found sufficient for aluminum (53), and 150 amperes for steel, in helping to reach a steady baseline. This, in turn, corresponds to heating rates of approximately 800°C/ms and 1100°C/ms respectively. Assuming a heating rate of 600-1200°C/ms as necessary for conditioning, required currents for various orifice diameters have been calculated using equation (28) and are shown in Table 12.

Table 12
Required Conditioning Currents to Aid the Attainment of a Steady Baseline in Steel

Orifice Diameter	Heating Rate 600	Heating Rate 1200 °C/ms
µm	Conditioning Current, amperes	
200	50	70
300	110	155
400	200	275
500	300	430
600	440	620

8. DISCUSSION I: ANALYSIS OF ERRORS

In the following sections, analysis of systematic (orifice expansion) and random (sampling and coincidence) errors associated with the particle counts of the system so far described is discussed from a number of perspectives. To provide a working basis for the error estimation, the first section is devoted to the estimation of the likely size distribution of inclusions in steels of varying cleanliness.

8.1. Range of inclusion Size Distributions in Molten Steel

Extensive research has been carried out by Flinchbaugh (44-46) and others (47-49) on the typical size distribution of inclusions extracted from aluminum killed plain carbon steels. An aqueous Coulter Counter was used to size the extracted particles. Flinchbaugh's techniques apply to both micro-inclusions, within the size range 3-40 microns, and macro-inclusions within 40-200 microns. His results showed that, on the basis of 250 g samples taken from different batches of steel, all those containing 50-70 ppm total oxygen had similar size distributions and when fitted into a power law relationship of the type

$$N_d = A\,d^{-k} \qquad (29)$$

where Nd is the number of inclusions greater than size d (per gram) and d is the inclusion size (microns); similar constants (A) and exponents (k) were found for the size region 40-200 microns. From his data an average value for the exponent (k) was 4.5±0.5 and for the constant $\text{Log}_{10}(A)$ was 8.5±0.9 within ±2 standard deviations based on an analysis of five steel samples.

Closer examination of his data reveals a systematic increase in (k) as defined by:

$$k = -\delta\ \text{Log}(N_d) / \delta\ \text{Log}(d) \tag{30}$$

with (d). A logarithmic plot of k vs. d shows a reasonably good linear relationship, suggesting a more general size distribution relation of the type:

$$k = A_1\ d^n \tag{31}$$

Integration of equation (31) gives an exponential distribution of the form

$$N_d = N_0\ \exp(-Bd^n) \tag{32}$$

where $B=A_1/n$. Equation (29) is a special case of equation (32) when n=0. The exponent (n) is then a measure of deviation of the size distribution curve from the power law. Exponent n=1 has also been suggested in the literature (35).

To find a hypothetical distribution that is as close to reality as possible, then, exponent (n) has been evaluated by a least square fit from the logarithmic plot of k vs. d. (B) and (N_o) are found by taking V_{43}=0.04xVf and N_{4o}=20 where V_{43} is the volume fraction of inclusions greater than 43 microns and Vf is the total volume fraction of oxides. The data used in this analysis were taken from Flinchbaugh's report (45) and the conversion of size distribution into volume fractions is explained in Appendix II. The results are then extrapolated to cover a size range of 10-1000 microns, and the final distribution is given in Table 13 and Figure 30. Figure 30 also provides the original data points for which the analytical equation (32) was made to fit. The lower end of the extrapolation gives good agreement with the measured values, a comparison being made in Table II.2. This then, is considered to be a likely distribution of oxide inclusions for an aluminum killed steel containing 50-70 ppm total oxygen. It should be emphasized that this analysis is not meant to replace the inclusion detection techniques but rather to give an order of magnitude analysis for the typical number of inclusions that can be expected in real practice. Its usefulness will become apparent in the following sections, in analysing the expected count errors associated with an electrical sensing zone instrument to be used in liquid steel.

To estimate particle size distributions for cleaner steels, the best ladle practices in Japan containing 10 ppm total oxygen is next considered as an example. A simple approach would be to reduce the number of inclusions by a factor given by the ratio of

Table 13
Oxide Inclusion Size Distribution of Steel Containing 50 ppm Total Oxygen, Based on Equation (31):

$n=0.322$
$B=4.1$
$N_0=14.3\times10^6$

Inclusion Diameter, d, µm	Number Greater than d per g	kg	ton	100 ton	Vd/Vf	k
10	2563				23.7 %	2.8
20	296				14.1	3.5
30	66				8.7	4.0
40	20				5.6	4.3
50		7327			3.7	4.7
60		3052			2.5	4.9
70		1397			1.7	5.2
80		687			1.2	5.4
90		358			0.88	5.6
100		196			0.64	5.8
120		66			0.35	6.2
150		16			0.16	6.6
200			2118		.048	7.3
300			90		.007	8.3
400				738	.001	9.1
500				90		9.8
600				14		10.4
700				2.7		10.9
800				0.6		11.4
900				0.2		11.8
1000						12.3

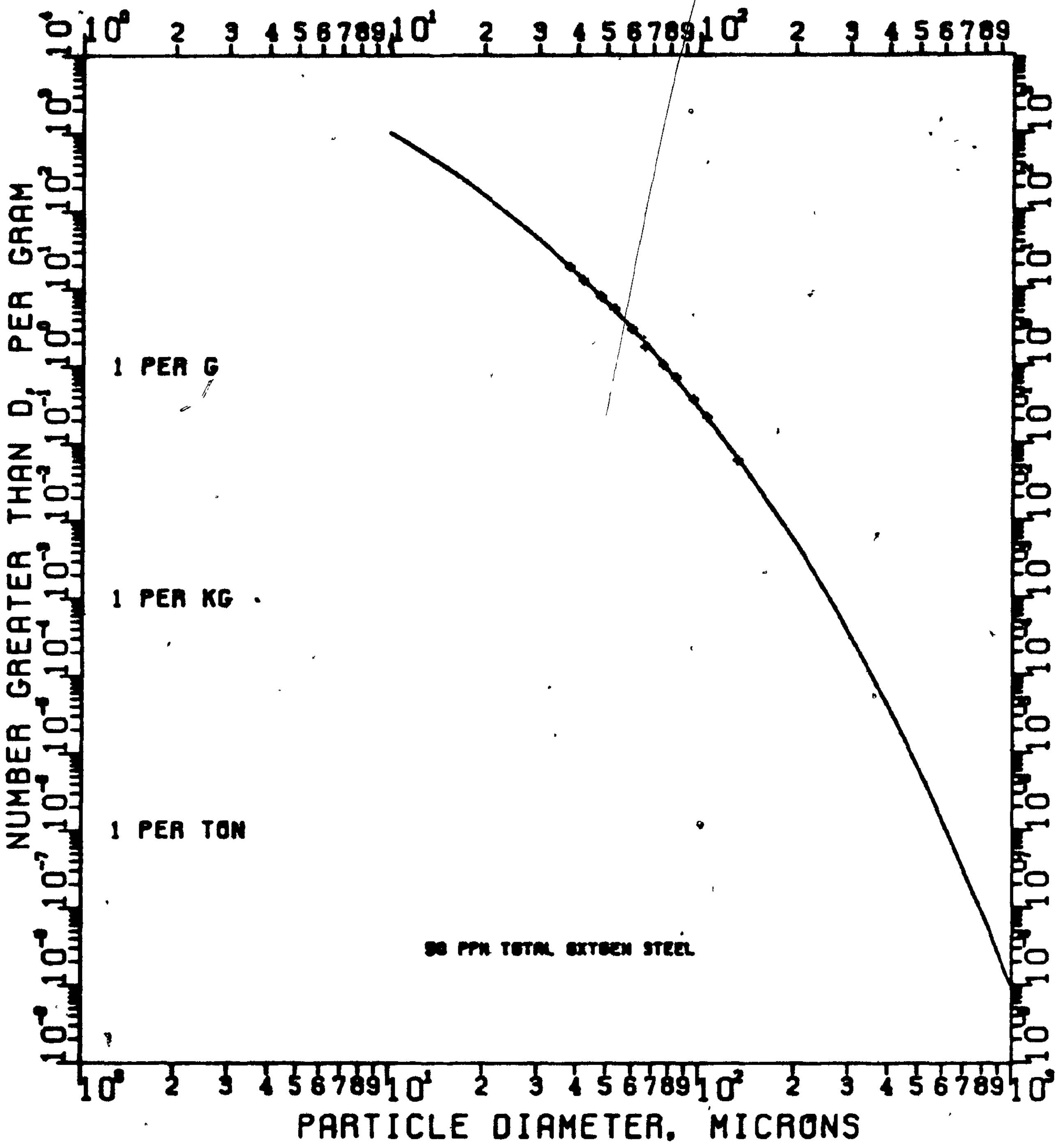

Figure 31 Plot of the oxide inclusion size distribution of steel in Table 13, including the original data points in ref. (45).

Table 14
Oxide Inclusion Size Distribution of Steel Containing 10 ppm Total Oxygen, Based on Equation (31):

$n=0.322$
$B=4.9$
$N_e=14.3x10^6$

Inclusion Diameter, d, μm	Number Greater than d per					
	g	kg	ton	100 ton	Vd/Vf	k
10	511				16.6 %	3.3
20	40				7.3	4.1
30	7				3.6	4.7
40		1612			1.9	5.2
50		490			1.0	5.5
60		173			0.6	5.9
70		68			.37	6.2
80		30			.23	6.4
90		14			.15	6.7
100		7			.10	6.9
120			1814		.04	7.4
150			332		.02	7.9
200			31		.003	8.6
300				73		9.9
400				4		10.8
500				0.3		11.6
600						12.3
700						
800						
900						
1000						

Table 15
Inclusion Size Distribution of a Steel Containing 1 ppm O as Al_2O_3 and 1 ppm S as MnS Inclusions, Based on Equation (31):

$n=0.322$
$B=5.6$
$N_0=14.3\times10^6$

Inclusion Diameter, d, µm	Number Greater than d per					
	g	kg	ton	100 ton	Vd/Vf	k
10	114				13.3 %	3.8
20	6				4.3	4.7
30		786			1.6	5.4
40		155			0.7	5.9
50		40			0.3	6.3
60		12			.17	6.7
70		4			.09	7.1
80			1582		.05	7.4
90			652		.03	7.7
100			287		.02	7.9
120			65		.007	8.4
150			9		.002	9.0
200				61		9.9
300				1		11.3
400				0.03		12.4
500						13.3
600						
700						
800						
900						
1000						

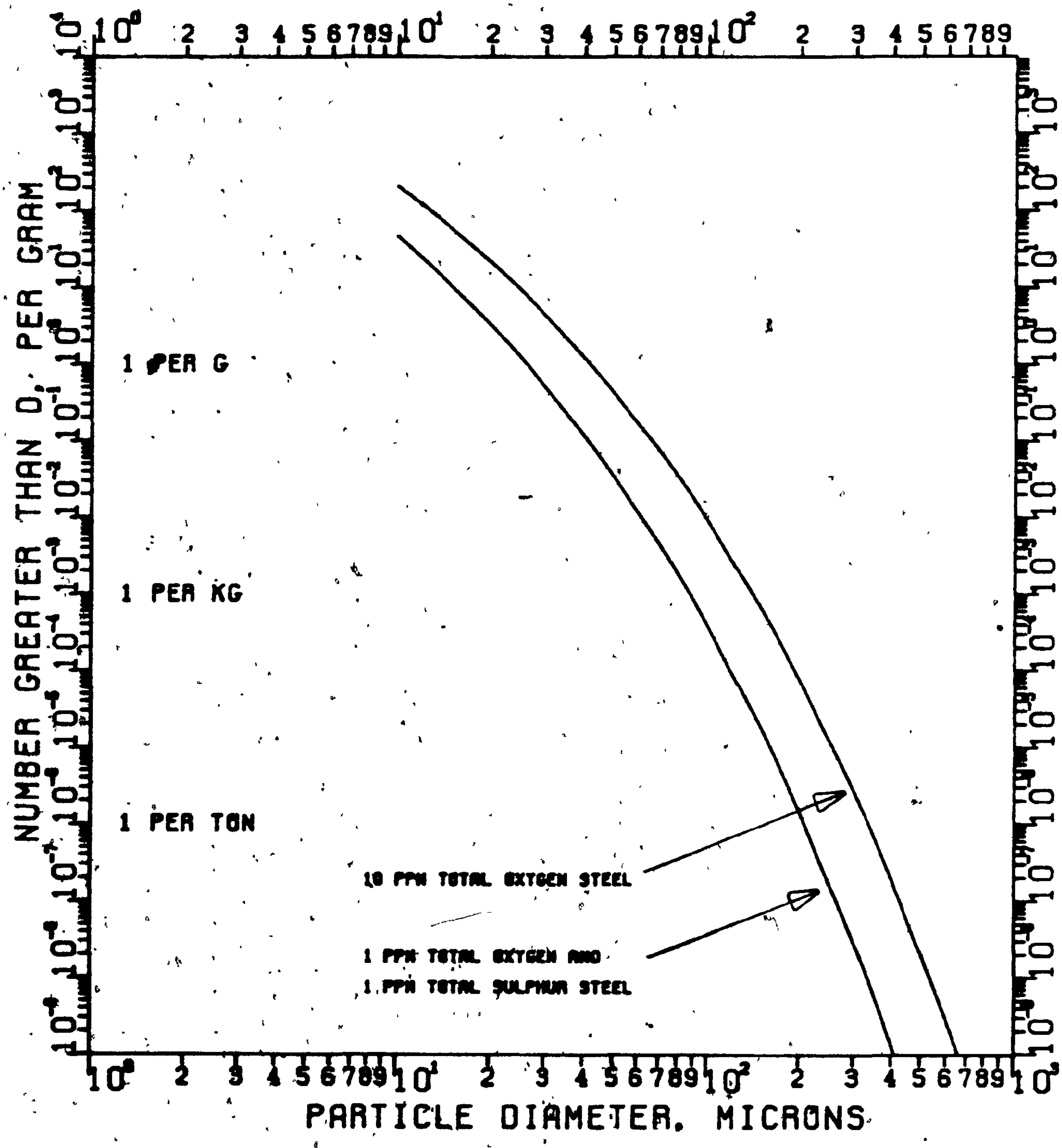

Figure 32 Plots of inclusion size distributions of steels in Tables 14 and 15.

the total volume fraction of inclusions in both steels. This will satisfy the mass balance requirement and effectively is equal to the reduction of the constant (N_o) by that factor. However, as the steel becomes cleaner, the larger inclusions are removed first. The net effect of this is a general increase in the value of (k). The value of (N_o) is therefore assumed to remain unchanged since the larger inclusions constitute a very small fraction of the total number. Observations also support this, when steel is made cleaner by electroslag remelting for instance, similar or even increased K1 values have been reported in the refined product (20).

At some inclusion diameter (d') however, the number greater (Nd') will be reduced exactly by the volume fraction ratio of the inclusions. The new value of (B) is then calculated by taking d'=10 microns. The exponent (n) is left unchanged as this only gives an indication of the discrepancy from the power law distribution. The new size distribution is shown in Table 14 and Figure 31.

Finally, an aluminum killed "superclean steel", first suggested by Kiessling (28) to demonstrate the composite nature of steel, containing 1 ppm oxygen as alumina inclusions and 1 ppm sulphur as MnS inclusions can be considered. This level of cleanliness is quite impracticable to attain in bulk quantities by today's practices. The estimated likely inclusion distribution is shown in Table 15.

8.2. Effect of Sample Volume on the Accuracy of Results

If the inclusions are randomly distributed in the melt, then Poisson's distribution applies for the number of inclusions in the samples taken. Accordingly then, the standard deviation of the observed counts is given by the square root of the number counted. As count rate increases for inclusions greater than a certain size, the accuracy of the results also increases. A count rate of 100 for instance, gives an estimate of the average number in the population to within 100±20 with a 95% confidence limit. Although in the present experiments samples of only 10 second duration were taken, it is possible to add these so as to obtain a larger sample volume which, in one aspiration, could equal the volume taken by the sampling cell, 50 mℓ (350 g) with the present probe. A recommended procedure might be to take 10 second samples and add them if they contain no stray peaks, but only resistive pulses.

By taking a 300 g sample of 50 ppm total oxygen steel and referring to Table 13, on average, 100 inclusions will be counted of sizes greater than 90 microns giving a reasonably accurate means for its assessment, and 10 inclusions greater than 150 microns and only 1 inclusion greater than 200 microns. For the assesement of larger inclusions that might still exist in the ladle, a much larger sample volume is needed. As for the clean steels and the super-clean steel it should, based on the hypothetical distributions from Tables 14 and 15, still be possible to detect inclusions as great as 110 and 70 microns respectively. This also illustrates, in an approximate way, the measuring power of the instrument: no matter how clean the steel is, there will still be a number of inclusions detected.

Limitations of sample volume also apply to other methods of inclusion measurement, particularly to those that depend on surface examination. The present instrument provides a 3 order of magnitude improvement in this respect.

Using the hypothetical distributions from Tables 13, 14 and 15, it is also possible to calculate the likelihood of orifice blockage for a given orifice diameter. For a 300 micron orifice for instance, the chances of having a particle greater than 300 microns in a 300 gram sample can be calculated as follows: Taking the case of 50 ppm total oxygen steel, from Table 13; the average number of particles greater than 300 microns in a 300 gram steel sample would be $\epsilon=(300)\times(90\times10^{-6})=0.027$. The probability of finding (r) number of particles in a sample volume that contains an average of (ϵ) number of particles is given by the Poisson's distribution, which states that:

$$P(r) = \epsilon^{r} e^{-\epsilon} / r! \qquad (33)$$

Therefore, the probability of not finding the large particle is:

$$P(r=0) = \epsilon^{0} e^{-\epsilon} / 0! = e^{-\epsilon} \qquad (34)$$

or of finding it then:

$$P(r \geq 1) = 1 - e^{-\epsilon} \qquad (35)$$

For the above example, this would be 2.7%.

The probability of blockage for other orifices and for the three types of steel considered are given in Table 16. If an acceptable probability for blockage is taken as 1% and assuming that blockage occurs by the presence of a large single particle rather than by the accumulation of small particles, then a 400 micron orifice is expected to perform well in an aluminum deoxidised steel, containing 50 ppm total residual oxygen.

8.3. Systematic Errors Induced by Expansion of Orifice Aperture

A major source of error in particle size measurements was the systematic expansion of the BN orifice during sampling. This appears to be in the order of 20 microns for cast iron and 30 microns for a low carbon steel, per aspiration. Only in one experiment with a boron-silicon steel was there no measurable orifice expansion.

The effect of orifice expansion will be two fold on the observed number of counts: the increased sample volume will tend to increase the number of counts while the worsened detection limit will tend to decrease it. An estimate of the error can be made for a 400 micron orifice for example, that expands to

Table 16
Probability of Blockage for Different Orifices in Different Steels of Varying Cleanliness

Orifice Diameter	Type of Steel		
	Table 13	Table 14	Table 15
μm	probability of blockage, %		
200	47	0.9	0.02
300	2.7	0.02	-
400	0.2	-	-
500	0.03	-	-
600	-	-	-

430 microns at the end of sampling as follows:

1. Error due to increased sample volume: the increase in the observed counts from the true counts, i.e. the counts if the orifice had remained at 400 microns, will be given by:

$$N_{ob} = (430/400)^2 N_T \tag{36}$$

$$N_{ob} = N_T + 0.15 N_T$$

2. Error due to not counting smaller particles: because the detection limit of the instrument set for the smallest particles of interest will increase in proportion to $(430/400)^{4/3}$, there will be less of the smaller particles counted at the Lower Level of Detection.. Assuming that a power law relationship for the size distribution applies within a narrow range at the average L. L. D. of 20 microns, then from Tables 13-15, k=3.5-4.5. The estimated decrease in the true counts will be given by:

$$N_{ob} = \{(430/400)^{4/3}\}^{-k} N_T \tag{37}$$

$$N_{ob} = N_T - (0.30 \text{ to } 0.35)\ N_T$$

Thus, the net effect of orifice expansion will be a 15-20% decrease in the number of total counts. Since the orifice expands gradually, the actual net effect will be approximately one half.

8.4. Random Errors

Random errors in the measuring system can arise from:

i. sampling errors

ii. coincidence effects

iii. variations in metal flow rate other than that due to orifice enlargement and variations in the current.

The first of these has already been dealt with in Section 8.2. The second arises from the presence of two or more particles in the sensing zone at the same time and has been described in the literature in relation to the Coulter Counter and other sensing zone instruments (81). So-called primary coincidence occurs when two particles above the detection limit enter the sensing zone at the same time, and are recorded as a single larger particle, thus lowering the number of observed counts. Secondary coincidence likewise occurs when two particles below the detection limit giving rise to a detectable peak, thus increasing the observed counts.

An estimate for the two effects can be made using Poisson's probability distribution and the size distribution in Table 13 as follows:

1. Primary Coincidence

Using a 0.4 mm diameter, 0.5 mm long orifice at a detection limit of 20 microns for example, the effective volume of the sensing zone may be calculated as $\sigma=0.063$ mm^3 and the average number of detectable particles in the sensing zone is then $\epsilon=0.13$. The probability of finding one or more particles in the sensing zone is given by equation (35), and this is equal to the probability of having a resistive pulse at the orifice, $P(r\geq1)=0.12$. If particles appeared one by one, the probability of having a particle at the orifice would have been equal to (ϵ). Since these probabilities are directly proportional to the observed counts and the true counts respectively, the observed counts will be reduced by:

$$N_{ob} = [P(r\geq1)/\epsilon]\ N_T \tag{38}$$

$$N_{ob} = N_T - 0.06\ N_T$$

2. Secondary Coincidence

Since voltage pulses are proportional to the particle diameter cubed, a particle with a diameter $(1/2)^{1/3}$x20=16 microns will produce a pulse that is one half of the pulse produced by a 20 micron particle. Therefore, continuing with the same example, when two particles within the size range 16-20 microns appear at the same time at the orifice, secondary coincidence will occur. The average number of 16-20 micron particles at the orifice is

$\epsilon'=0.15$. The probability of having two or more particles within that size range is then:

$$P'(r\geq 2) = 1 - P'(r=0) - P'(r=1) \tag{39}$$

$$P'(r\geq 2) = 1 - e^{-\epsilon'} - \epsilon' e^{-\epsilon'} \tag{40}$$

$$P'(r\geq 2) = 0.01$$

A further refinement may be made by considering 3 or more particles in the size range that give rise to 1/2 to 1/3 of the minimum detected pulse (16 to 14 microns) and so on. The probability of this second order effect can be calculated to be $P''(r\geq 3)=0.0005$ and becomes insignificant at higher orders. The sum of these probabilities give the probability for secondary coincidence:

$$P(S.C.) = P'(r\geq 2) + P''(r\geq 3) + \ldots \tag{41}$$

The secondary coincidence effect on the observed counts is then:

$$N_{ob} = N_T + [P(S.C.)/\epsilon]\, N_T \tag{42}$$

$$N_{ob} = N_T + 0.09\, N_T$$

For the case considered therefore, the net effect of primary and secondary coincidence will be a 3% increase in the observed counts. The effect will diminish as a steel becomes cleaner. For the 10 ppm total oxygen steel in Table 14 for instance, the net increase in counts because of coincidence would be 1%, and for the measured size distribution in Figure 22-A, approximately 2%, assuming a moderate concentration of 40 inclusions per gram in the size range 21-26.5 microns.

In order to be able to estimate secondary coincidence effects, an estimate of inclusion concentration below the detection limit is necessary. Size distributions in Tables 13 and 14 therefore provide a convenient starting point to give an order of magnitude values for the distribution of alumina inclusions in different steels.

9. DISCUSSION II: GENERAL CONSIDERATIONS

In this chapter, the major problems that have been encountered during particle detection experiments in steel baths and the possible causes for these are discussed. Basically an attempt is made to illustrate the related phenomena that are interacting to possibly produce the observed difficulties.

9.1. Potential Vaporisation / Cavitation of Melt during Use of Conditioning Current

"Cavitation" as a term is primarily used to describe the ejection of gas phase from a liquid as a result of pressure reduction (82). Reference has already been made in Subsection 6.2.2 to the possibility of cavitation in accounting for the difficulties observed in cast iron. A close examination of the sensing zone environment reveals a number of other factors that can lead to this phenomena.

9.1.1. Effect of Velocity Distribution on Heat Dissipation in the Electrical Sensing Zone

Figure 33 shows the effect of 150 amperes of conditioning current on a 300 micron diameter, 0.5 mm long orifice, where average residence times and temperatures of molten iron over a cross-section at the entry, middle and exit of the orifice are superimposed. Although the flow is laminar, it will not be fully developed and a centerline velocity at the exit for L/D=1.67 can

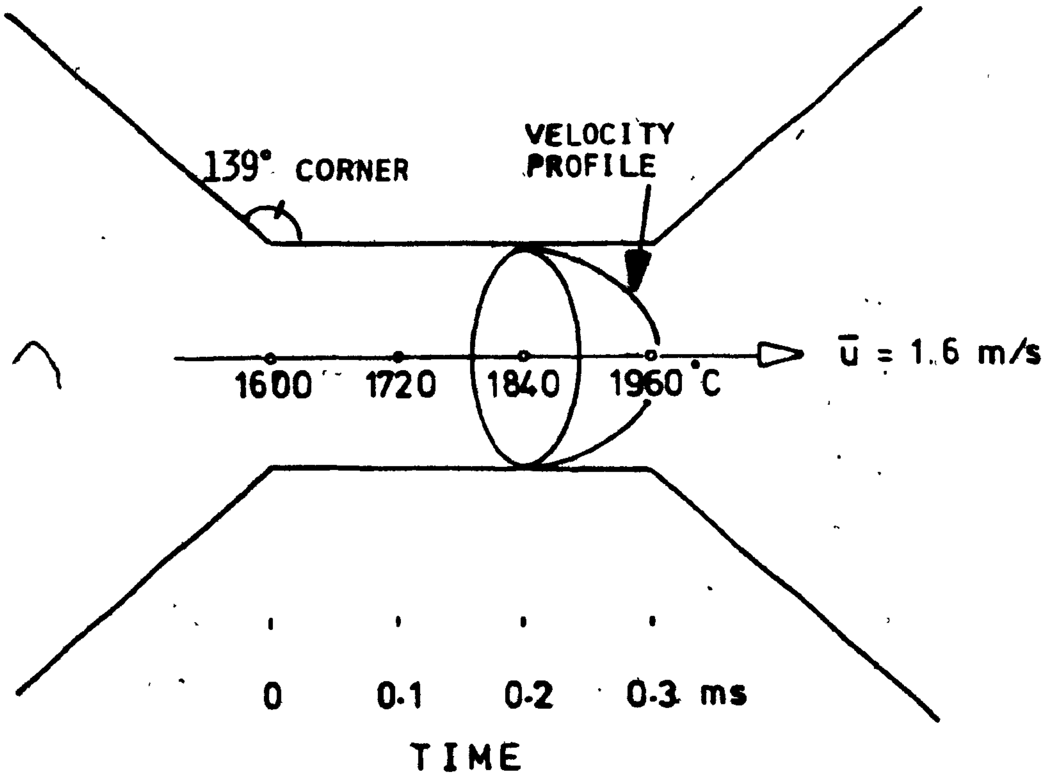

Figure 33 Heating effect of 150 ampere conditioning current on a 300 micron diameter, 0.5 mm long orifice.

be calculated to be $1.25\mathrm{x}\bar{u}=2.0$ m/s (83). There will nevertheless be a radial velocity gradient and this will be more pronounced towards the exit. As a result, because of the increased residence time, fluid near the orifice wall will be heated up considerably more than the average over a given cross-section perpendicular to the centerline flow.

9.1.2. Effect of Electric Field around Sharp Corners

The artefact peaks observed in the Coulter type counters because of off-axis trajectories have prompted researchers to investigate the variation in electric potential gradient at an orifice mouth (84,85). Both experimental and computational results indicate a sharp increase in the potential gradient near sharp corners which theoretically becomes infinite at the edge of a 90° corner. The computational results of Wilson (85) for bevelled edges with 135° corners, which are geometically similar to the countersunk BN orifice used, predict two to three-fold increase in the value of total potential gradient near the corner. Since the volumetric heat generation is given by:

$$S = E^2/\rho \qquad (43)$$

this would reflect a 4 to 9 fold increase in the rate of temperature rise near the peripheral edges of the orifice entry and exit.

9.1.3. Pinch Effect

The "pinch effect" is an electromagnetic phenomenon observable at high current densities when the loop component of the magnetic field generated by the current itself exerts a radial compressive pressure to the current carrying medium. The pressure increases along radial direction towards center and its value at the surface of a cylindrical conductor can be shown to be:

$$P' = B^2/2\mu_0 \tag{44}$$

where B is the magnetic flux density at the surface and μ_0 is the permeability of the free space (85). Magnetic flux density is related to the total current flowing through a cross section by the integral result of Biot-Savart law:

$$B = \mu I/\pi D \tag{45}$$

for cylindrical conductors, where μ is the permeability of molten iron which is approximately the same as that of the free space: $\mu=4\pi x10^{-7}$ H/m. Using equations (45) and (44) and Table 12, pinch pressures can be calculated for the suggested conditioning currents and are given in Table 17. The effect becomes more pronounced at larger diameters because the suggested conditioning currents increase in proportion to the square of the orifice diameter.

Table 17
Order of Magnitude of Pinch Pressures for the Suggested Conditioning Currents in Table 12

Orifice Diameter	Heating Rate, °C/ms 600	1200
μm	Pinch Pressure, kPa	
200	4	8
300	9	18
400	16	32
500	25	50
600	36	72

$$P = (2\text{x}10^{-7}/\pi)\ I^2/d^2 \quad \text{Pa}$$

Because current densities used in equation (28) to estimate the rate of temperature rise are proportional to I^2/d^4, pinch pressures increase in proportion to d^2.

The total pressure within the fluid at a point will then be the sum of the hydrostatic pressure and dynamic pressures and the pinch pressure, whose net effect will be a state of compression. Consequently, at the surface, the fluid will tend to break away from the orifice wall and this will happen when the pinch pressure exceeds the hydrostatic pressure.

9.1.4. Lowered Hydrostatic Pressure at Orifice Exit

Because of the laminar nature of the flow, the jet at the orifice exit may recover some of its specific kinetic energy before it finally dissipates into the surrounding fluid of pressure P_2. Therefore, the exit pressure of the orifice may be lower than P_2, but not less than $(P_2-\rho u^2/2\alpha)$ or approximately $2\Delta P$ gauge vacuum, assuming that all kinetic energy at the exit recovers to pressure energy. The net total mechanical energy loss of the fluid in going from 1 to 2 is $Ef=(P_1-P_2)/\rho$

9.1.5. Formation of Gaseous Reaction Products

Possible formation of CO from the reaction of solute carbon and a silica particle has already been discussed in the Subsection 6.2.2. A likely place for the nucleation of a gaseous product would be the high temperature, low pressure region of the orifice wall, particularly towards the exit.

It has been suggested that there are 10^5 to 10^7 oxide inclusions in a gram of steel (17), which gives a mean particle distance of 100 to 25 microns respectively between inclusions. This gives sufficient opportunity for adsorption of submicroscopic inclusions to the orifice wall, provided that surface conditions are favourable.

If gaseous reaction products nucleate at the orifice wall, they may then grow into gas pockets at the exit edge. Any reduced cross sectional area of the fluid would increase the pinch pressure to allow for further expansion of the gas pocket. Also, because of the increased heat towards the final snap, one can speculate that more iron and other solutes will evaporate to fill the gas pocket. Once separation occurs, surface tension will try to keep the new surfaces seperate.

9.2. Baseline Instability

Baseline instability proved to be a major difficulty in the development of the instrument. It appeared as oscillations and at worst as spikes and random noise.

9.2.1. Oscillations

These appeared sometimes in cast iron and at a critical velocity in mercury experiments. The very regular nature of these oscillations suggests that an explanation should be possible. If the critical flowrate in mercury corresponds to the formation of a circulating eddy at the orifice entry, this will provide a radial, cross-stream, up and down motion which cuts the loop component of the magnetic field and hence will give rise to an e.m.f. on either side of the orifice. Taking the metal velocity as 1 m/s, the period of the oscillations will be 1 ms. This hypothesis correctly predicts the frequency and direction of the e.m.f.'s and explains why the oscillations dissappear when current is turned off; however, it does not give a good value on their magnitude: referring to Figure 34, if the metal velocity within the eddy is 1-10 m/s, the maximum thickness of an eddy would be approximately 100 microns, so that for 20 amperes passing through a 300 micron orifice, Bmax is 0.03 Wb/m², then the e.m.f. generated will be 10 microvolts maximum, assuming that a mass concentration exists within the eddy in order not to be self cancelling. The observed magnitude of the oscillations on the other hand were hundreds of microvolts and a similar transition also occurs in water where the self generated magnetic field of the current would be negligible.

Another hypothesis that has been suggested is the periodic slip of the fluid at the orifice wall near entry because of a recirculating eddy, thereby momentarily reducing the orifice area (87).

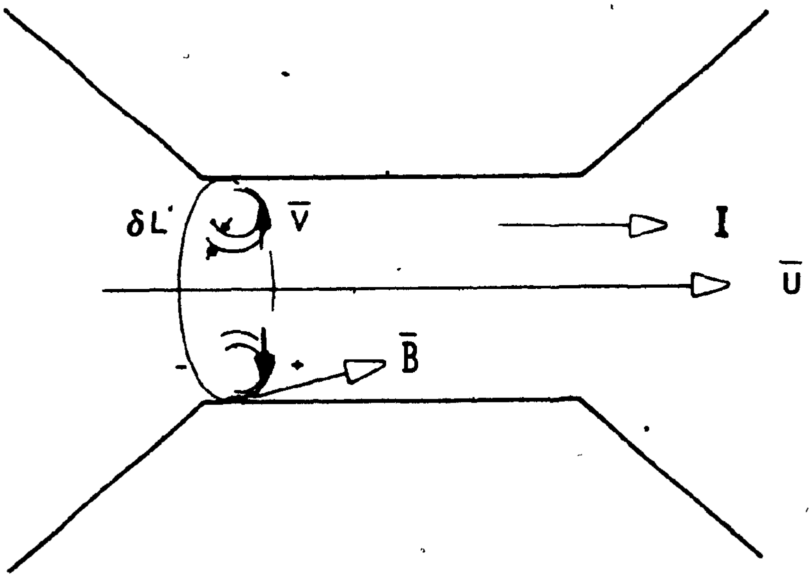

MAGNETIC FLUX DENSITY AT THE WALL: $\bar{B} = \frac{\mu}{\pi}\frac{I}{D}$

MAXIMUM E.M.F. GENERATED BY THE RECIRCULATING EDDY: E.M.F.' = $\bar{V} \times \bar{B} \cdot \overline{\delta L}$

Figure 34 Generation of e.m.f. by a recirculating eddy at the orifice mouth.

9.2.2. Spikes and Random Noise

Figures 22 and 35 show examples of "spikes" and random noise. The spikes occured in the positive direction and were usually accompanied by an unsteady current. Their presence indicated that something was seriously wrong at the orifice or at the tips of the electrodes.

Random noise, such as is shown in Figure 35-(A) could be the result of a switching action in the electrical line. Fortunately the high frequency noise of the type shown in Figure 35-(A) does not activate the pulse detector so that is not counted in the MCA.

A complete loss of current, or when current drops to less than about 10% of its nominal value, will produce an oscilloscope image of the type shown in Figure 35-(B).

9.3. Erosion of the Boron Nitride Orifice

Since boron nitride is soft and susceptible to oxygen, its deterioration could be the result of both mechanical and chemical erosion. However, the fact that at least in one experiment with boron silicon steel containing some amount of aluminum there was no measurable orifice expansion suggests that chemical erosion is the more important mechanism. The dissociation of BN in molten

COLOURED PICTURES
Images en couleur

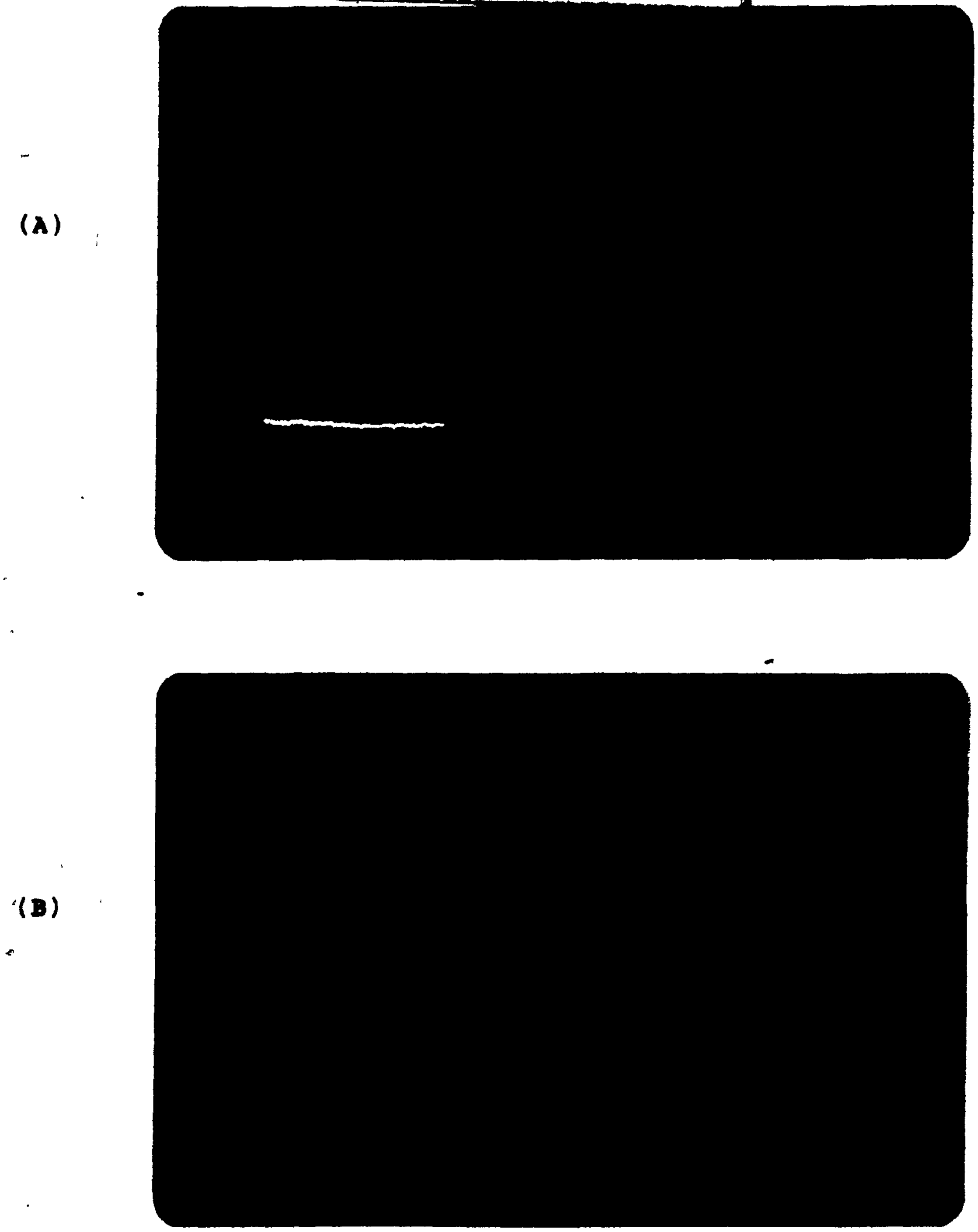

Figure 35 Random noise. (A) High frequency noise possibly generated by switching action in the electrical line. (B) Oscilloscope display when current is unsteady because of imperfect electrical contacts.

iron will be largely determined by the following reaction:

$$2\ BN + 5\ \underline{O} = B_2O_5 + 2\ \underline{N} \qquad (46)$$

Thus chemical erosion depends on the dissolved nitrogen and oxygen contents of the steel. Carborundum's grade HP BN is stable to >2775°C under neutral or reducing atmospheres. Hence, dissociation by way of the reaction:

$$BN = \underline{B} + \underline{N} \qquad (47)$$

is less likely. Under oxidising conditions, the manufacturer's recommended upper temperature limit for use of use is 1200°C. Its rate of dissociation most likely depends on the oxygen potential and the temperature of the system.

10. CONCLUSIONS AND CLAIMS TO ORIGINALITY

This is the first time inclusions have been detected and counted directly in molten steel and cast iron on a one to one basis.

The detection method used is based on resistive pulse counting of individual samples passing through an electrical sensing zone, commonly known as the "Coulter Counter" in aqueous media. Potential use of this method can provide an accurate and rapid means for steel cleanliness to be measured in its final stages of processing before solidification. This implies a chance for corrective actions to be taken in production.

To date the instrument has been developed to perform satisfactorily for low temperature alloys of iron. Further development of the sensing zone, particularly with regards to orifice shape is expected to be important for the stable operation of the instrument. Orifice enlargement seems to be the major area that will need improvement, either by the use of special refractories or by some sort of real time signal processing to compensate for the effect of orifice expansion.

APPENDIX I

RESISTIVE PULSES CAUSED BY PARTICLES WITHIN AN ELECTRICAL SENSING ZONE

DeBlois and Bean (59) have shown that for small particles, a relation first proposed by J. C. Maxwell (88) can be used to derive an expression for ΔR. Maxwell showed that the effective resistivity of a conducting fluid containing a dilute suspension of insulating spheres can be expressed as

$$\rho_{eff} = \rho_e (1 + 3/2\ V_f + \ldots) \qquad (48)$$

where Vf is the volume fraction of the spheres. For a cylindrical sensing zone of length (L), and diameter (D), filled with a fluid of resistivity (ρ), the resistance is:

$$R_e = \rho_e L/A = 4\rho_e L/\pi D^2 \qquad (49)$$

When a spherical particle is introduced into the sensing zone, its volume fraction becomes:

$$V_f = V_{sphere} / V_{cylender} = (\pi d^3/6)/(\pi D^2 L/4)$$

$$V_f = 2\ d^3 /\ 3\ D^2 L \qquad (50)$$

Substituting (49) into (47) into (48) gives the resistance of the sensing zone with the particle in it.

$$R_1 = (4/\pi)(\rho_e L/D^2)(1+d^3/D^2L + \ldots) \tag{51}$$

Subtructing (48) from (50) gives the desired expression for ΔR:

$$\Delta R = 4\rho_e d^3/\pi D^4 \tag{2}$$

APPENDIX II

MATHEMATICAL DESCRIPTION OF INCLUSION SIZE DISTRIBUTION WITHIN STEEL MATRIX

II.1. Definitions

In general, there are two ways to describe particle size distributions: frequency distributions and cumulative distributions.

A histogram or a bar chart is a form of frequency distribution where number of particles within given size intervals are plotted against particle size in the form of rectangles whose lengths represent the frequencies and whose widths represent the size interval. In the limiting case when the interval becomes infinitely small, a continuous curve is obtained and the vertical displacement on the frequency distribution at a given particle size is then termed particle population density at size (d). For inclusions in steel, this may conveniently have the units of $g^{-1}.\mu m^{-1}$. The value of the particle population density which refers to the frequency of particles at size (d), may physically be interpreted as the number of particles, per gram, in a size interval of 1 micron at size (d) **had the frequency remained constant** in this interval.

A cumulative distribution on the other hand, refers to the number, volume or mass of particles less or greater than a given size in a given population. Since numbers greater than a certain size is of particular interest, the latter convention is adapted for inclusions in steel. Vertical axis in this case, may have the units of *numbers per gram* or *parts per million by volume.*

Figure I.1 schematically shows and compares the two distribution curves. Frequency for a given interval from d to d+δd is equal to N(d)-N(d+δd) on the cumulative distribution curve. Dividing this by the interval δd gives the particle population density at size d, in the limit when δd goes to zero. Hence:

$$N_{d\ \text{to}\ d+\delta d} = -(N_{d+\delta d} - N_d)/\delta d \qquad (52)$$

The minus sign arises because number of inclusions **greater than** size d is considered.

A similar argument applies also for the volume fraction distribution of inclusions. The notation used for the size distribution variables are included in the list of symbols. ND and VD are therefore related to the density functions by the following equations:

$$N_d = \int_d^\infty N_d\,\delta d \quad \text{or} \quad N_d = -\delta N_d/\delta d \qquad (53)$$

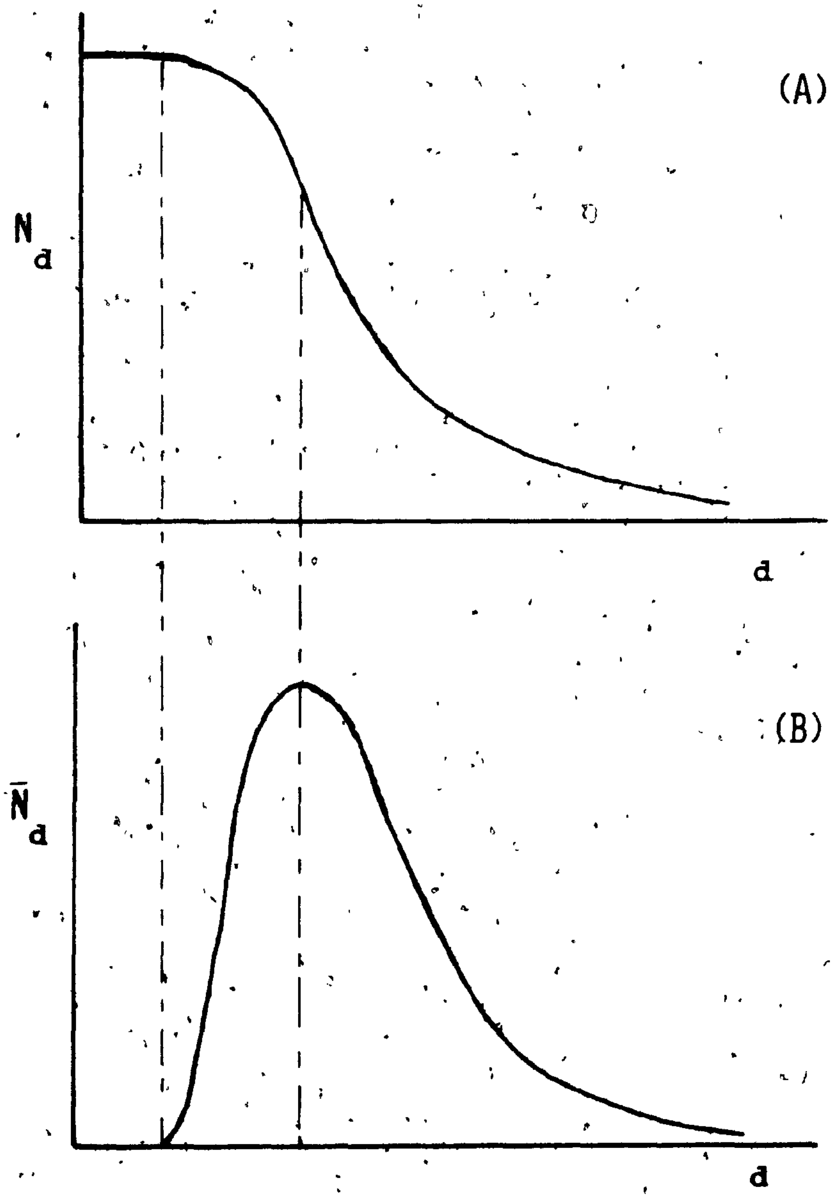

Figure II.1 Hypothetical size distribution curves illustrating the relationship between cumulative (A), and frequency (population density) (B) distribution.

$$V_d = \int_d^{\infty} \bar{V}_d \, \delta d \qquad \text{or} \qquad \bar{V}_d = -\delta V_d / \delta d \tag{54}$$

II.2. Conversion of Size Distribution into Volume Fraction Distribution

This is important in performing a mass balance on a given size distribution data. The binding relation is:

$$\bar{V}_d = (\pi d^3/6)\, \bar{N}_d \tag{55}$$

which states that the volume fraction density at size d is equal to the volume of inclusion times the number of inclusions at size d.

II.3. Conversion of Chemical Analysis into Volume Fraction of Constituent Inclusions

Since oxygen and sulphur are virtually insoluble in steel at room temperature, any total amount given will represent the amount bound by inclusions. From a knowledge of constituent inclusion stoichiometry and its density, volume fractions can be obtained by:

$$V_f = \text{(volume of inclusions)/(volume of steel)} \tag{56}$$

for a unit mass of steel:

$$V_{incl} = \left[\frac{\text{M.W. of inclusion}}{\text{M.W. of bound O or S}} \bullet \text{wt fraction of O or S}\right] + \rho_{incl}$$

$$V_{Fe} = 1/\rho_{Fe}$$

for a unit weight fraction of oxygen and sulphur then:

$$V_f = \frac{\rho_{Fe}}{\rho_{incl}} \bullet \frac{\text{M.W.}_{inclusion}}{\text{M.W.}_{bound\ O\ or\ S}} \qquad (57)$$

Table II.1 gives a conversion of total oxygen or sulphur values (ppm) into volume fractions of typical inclusion phases encountered in steel.

II.4. Calculation of the Constants in Equation (32)

The size distribution used was:

$$N_d = N_0 \exp(-Bd^n) \qquad (32)$$

Value of n=0.322 was found from a least fit of Log(k) vs. Log(d), using Flinchbaugh's data (45). Again using his data: N_{40}=20 per gram, V_{43}=0.04xVf and Vf=212.5 ppm for 50 ppm total oxygen; values of B=4.1 and N_0=14.3x10^6 are calculated.

Table II.1
Conversion of Total Oxygen and Sulphur, ppm to Volume Fraction of Inclusions Vf, ppm

1 ppm of	within constituent inclusion	M.W.	density	Vf
			kg/m³	ppm
O	Al_2O_3	102	3900	4.25
	SiO_2	60	2800	5.22
	$MnSiO_3$	131	3500	6.08
	Mn_2SiO_4	202	3500	7.03
	$Al_2O_3.SiO_2$, kyanite	162	3247	5.06
	$3(Al_2O_3).2(SiO_2)$, mullite	213	3156	5.06
S	MnS	87	4000	5.30
	MnS_2	119	3460	4.20

Conversion of size distribution into volume fraction distribution is made in the following steps:

$$\bar{N}_d = -\delta N_d/\delta d = nBd^{n-1} N_d \qquad (58)$$

$$\bar{V}_d = (\pi d^3/6) \bullet nBd^{n-1} N_d \qquad (59)$$

$$V_d = (\pi/6)\, N_0 \int_d^{\infty} d^3 \exp(-Bd^n)\; nBd^{n-1}\; \delta d \qquad (60)$$

provided V_{1000} is negligible extrapolation to $d=\infty$ does not cause a serious error. Substituting $Y=Bd^n$ and $\delta Y=nBd^{n-1}\delta d$:

$$V_d = (\pi/6)(N_0/B^{3/n}) \int_Y^{\infty} Y^{3/n} \exp(-Y)\; \delta Y \qquad (61)$$

$$V_d = (\pi/6)(N_0/B^{3/n})\Big[\int_0^{\infty} Y^{3/n} \exp(-Y)\; \delta Y - \int_0^{Y} Y^{3/n} \exp(-Y)\; \delta Y\Big] \qquad (62)$$

The definite integral on the left has the value (3/n)! (89). Therefore:

$$V_d = (\pi/6)(N_0/B^{3/n})\Big[(3/n)! - \int_0^{Y} Y^{3/n} \exp(-Y)\; \delta Y\Big] \qquad (63)$$

for d>10 microns. The definite integral inside the brackets can now be numerically integrated. This equation is used to find a value for (B) by trial and error and to find the volume fractions in Tables 13, 14 and 15.

II.5. Comparison of the Lower-end of the Extrapolation in Equation (32) with Measured Size Distribution Data

Figure II.2 shows frequency (population density) distributions of oxide inclusions extracted from aluminum killed steels (46). In these figures, population density is defined as

$$N'_d = \delta N_d / \delta \mathrm{Log}(d) \quad \text{per gram} \qquad (64)$$

Using relations (52-54), a frequency distribution is calculated within 10 micron intervals and a total oxygen value is evaluated for each measured distribution. The results are compared with the calculated values from equation (32) in Tables II.2 and II.3.

As can be seen from the tables, agreement with 50 ppm oxygen is quite good. At 10 ppm level however, the indication is that more of the 10-40 micron inclusions are removed and the population density decline is not as steep.

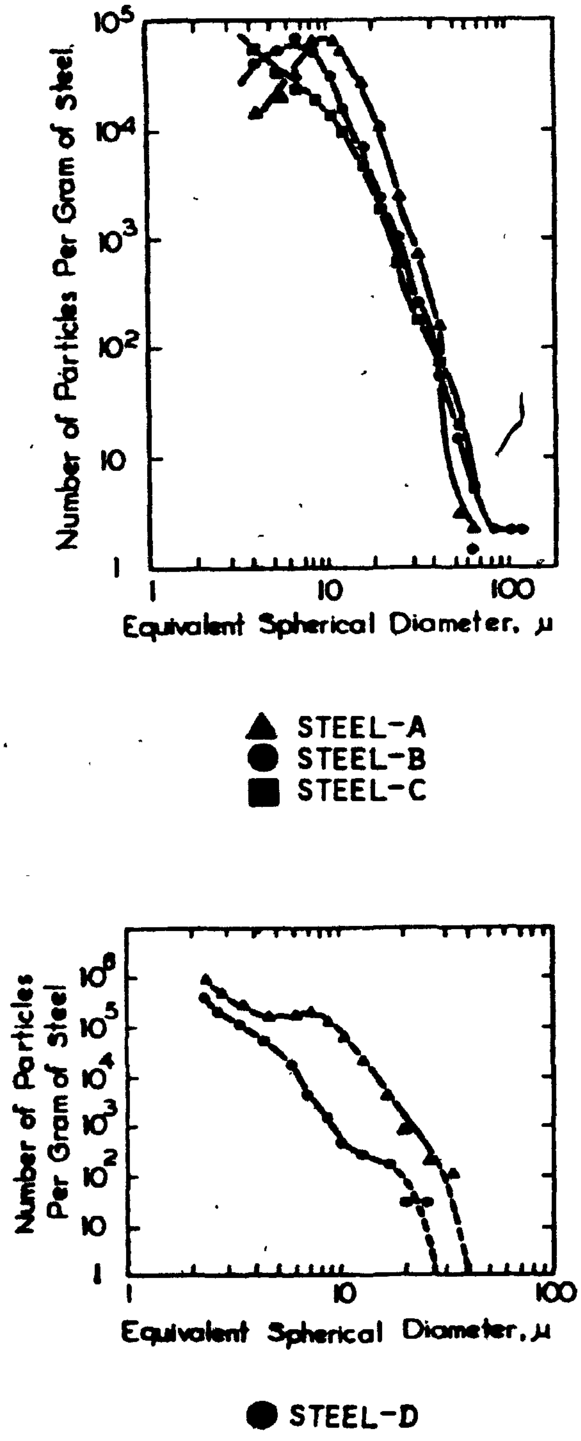

Figure II-2 Measured frequency distrbution of inclusions in various steels, after Flinchbaugh (46).

Table II.2
Comparison of the Frequency Distribution of Inclusions in Experimental Aluminum Killed Steels, Figure II.2 and Equation (32)

	Experimental Aluminum Killed Steels			Equation (32)	
	(A)	(B)	(C)		
Total Oxygen	100	50	30	50	ppm
Size Range					
µm	number of inclusions per gram				
40-30	80	30	24	46	
30-20	970	250	142	230	
20-10	9680	2420	2170	2267	
10-5	11000	9500	7500	11830	
5-3	2500	7300	13200		

Table II.3
Comparison of the Frequency Distribution of inclusions in a Commercial Al-Killed Steel, Steel (D) from Figure II.2 and equation (32)

	Commercial Al-Killed Steel	Equation (32)	
Total Oxygen	15	10	ppm
Size Range			
µm	number of inclusions per gram		
40-30	3	5	
30-20	5	33	
20-10	82	471	
10-5	2250		
5-3	16000		

REFERENCES

1. Chone J , "Surface Defects in Continuously Cast Stainless Steel in ref. 5, pp. 385-415, 1983

2. Sellars C M , "Static Recrystallisation and Precipitation During Hot Rolling of Microalloyed Steels", ASM Materials Science Seminar on Deformation, Processing and Structure, pp. 245-277, 23-24 Oct. 1982

3. Pickering F B , "The Spectrum of Microalloyed High Strength Low Alloy Steels", International Conference on Technology and Application of HSLA Steels, Philadelphia, Penn., pp. 1-31, 3-6 Oct. 1983

4. Production and Application of Clean Steels, International Conference at Balatonfured, Hungary, held on 23-26 June 1970, The Iron and Steel Institute, London, 1972

5. Clean Steel, Proceedings of the Second International Conference on Clean Steel, held on 1-3 June 1981 at Balatonfured, Hungary, The Metals Society, London, 1983

6. Sweedish Symposium on Non-metallic Inclusions in Steel, Eds. H. Nordberg and R. Sandstrom, arranged by the Uddeholm Research Foundation, Sweedish Institute for Metal Research, 27-29 April 1981

7. Inclusions, Ed. F. B. Pickering, Institution of Metallurgists, Monograph No. 3, Chameleon Press, London, 1979

8. Non-metallic Inclusions in Steel, Ed. R. Kiessling and N. Lange, Part I: ISI Special Report No. 90, London, 1964; Part II: ISI Special Report No. 100, London, 1966; Part III: ISI Special Report No. 115, London, 1968

9. Scaninject, International Conference on Injection Metallurgy, Lulea, Sweeden, 9-10 June 1977

10. Scaninject II, 2nd International Conference on Injection Metallurgy, Lulea, Sweeden, 12-13 June 1980

11. Scaninject III, 3rd International Conference on Refining of Iron and Steel by Powder Injection, Lulea, Sweeden, 15-17 June 1983

12. Ward R G , The Physical Chemistry of Iron and Steel Making, "Oxygen and Sulpher Potential Diagrams", pp. 58 and 59; "the Sulphur Problem", pp. 80, Edward Arnold, London, 1962

13. Turkdogan E T , Physical Chemistry of High Temperature Technology, Academic Press, 1980

14. Ototani T , "Methods for Refining Molten Iron and Steels", U. S. Patent No 4,094,666, 13 June 1978

15. Usui T et al., "Production of Line Pipe Steel for Sour Gas Services by Gas and Powder Injection", in ref. 10, pp.12.1-12.24, 1980

16. Bail C W , Department of Metallurgical Engineering, Ecole Polytechnique, Montreal, 1985

17. Miyashita Y , Tetsu to Hagane, Vol 52, pp. 1049-1060, 1966

18. Turkdogan E T , "Nucleation, Growth and Flotation of Oxide Inclusions in Liquid Steel", J. of Iron and Steel Institute, Vol 204, pp. 914-919, Sept. 1966

19. Turkdogan E T , "Deoxidation of Steel", J. Iron and Steel Institute, Vol 210, pp. 21-36, Jan. 1972

20. Fleischer H-J et al., "Investigations into the Degree of Cleanliness of Special Steels with Reference to Deformation by Rolling", in ref. 5, pp.10-21, 1983

21. Pickering F P , "The Need for Inclusion Assesment", in ref. 7, pp.182-198, 1979

22. Brookbank D and Andrews K W , "Stressfield Around Inclusions and their Relation to Mechanical Properties", in ref. 4, pp. 186-198, 1972

23. Emi T and Iida Y , "Impact of Injection Metallurgy on the Quality of Steel Products", in ref. 11, pp. 1.1-1.31, 1983

24. Wojcik W M et al., "Inclusion Counting of Steel Residues as Means of Assesing the Hot Working Performance of Steel", J. of Metals, Vol 19, Dec. 1967

25. Bengttson K , "Inclusions and Polishability", in ref. 6, pp. 450-462, 1981

26. Pomey G and Trentini B , "Introductory Address: Some Aspects of Cleanness in Steels", in ref. 4, pp. 1-14, 1972

27. Leach J C C , "Production of Clean Steel", in ref. 4, pp.105-114, 1972

28. Kiessling R , "Clean Steel - A Debatable Concept", in ref. 5, pp. 1-9, 1983

29. Nordberg H , in ref. 28, pp. 6, 1983

30. Techniques for Metals Research, Ed. R. F. Bunshah, Vol III, "Modern Analytical Techniques for Metals and Alloys", Part 1, pp. 69-139, Interscience, New York, 1970

31. Sutton W H and Clark I D , "Development of an Electron Beam Melting Test to Evaluate the Cleanliness of Superalloys", Conference on Electron Beam Melting and Refining, State of the Art 1983, Ed. R. Bakish, pp. 33-60, Bakish Materials Corp., 1983

32. -, "Standart Practice for Determining the Inclusion Content of Steel", American Society for Testing and Materials, Designation E45-84, 1984

33. Blank J R , "Methods for the Assessment of Non-metallic Inclusions in Steel", in ref. 7, pp. 199-216, 1979

34. Melford D A , "Automatic Cleanliness Assessment of Steel", in ref. 4, pp. 229-233, 1972

35. Lagneborg R , Ekelund S and Werlefors T , "Combined Image and X-Ray Analysis in Scanning Electron Microscopy for Automatic Multiparameter Characterisation of Non-metallic Inclusions", in ref. 5, pp. 39-62, 1983

36. Martensson H , "Report of the Jernkontoret Automatic Inclusion Assessment Committee", in ref. 4, pp. 235-240, 1972

37. Flinchbaugh D A , Homer Research Laboratories, Bethlehem Steel Corporation, Pa 18016, Personnal Communication, 1985

38. Smith C S and Guttman L , Trans TMS-AIME, Vol 197, pp. 447-452, 1953

39. Clark E E , "Ultrasonic Assessment of Plate Steel Cleanliness", in ref. 4, pp. 264-272, 1972

40. Cipywnyck H Z , "Internal Defect Detection", Steel Industry / Researcher, Sensor Research Workshop, Sponsored by CSIRA and CANMET, pp. 21-27, May 1984

41. Hutchins D A , "Non-contact Methods for Ultrasonic Inspection of Steel", in ref. 35, pp. 29-32, 1984

42. Allan C J and Tonner P D , "Tomography - an Overview of the CNRL Program", in ref. 35, pp. 61-68, 1984

43. Smerko R G and Flinchbaugh D A , "Recent Progress in the Chemical Extraction of Non-metallic Inclusions", Journal of Metals, Vol 20, pp. 43-51, July 1968

44. Flinchbaugh D A , "Expanded Capability of the Coulter Counter with a New Aperture Apparatus", Analytical Chemistry, Vol 43, No 2, pp. 172-175, 1971

45. Flinchbaugh D A , "Use of a Modified Coulter Counter for Determining Size Distribution of Macroinclusions Extracted from Plain Carbon Steels", Analytical Chemistry, Vol 43, No 2, pp. 178-182, 1971

46. Flinchbaugh D A , "Determining Size Distribution of Oxides in Plain Carbon Steels by Halogen-in-Organic Solvent Extraction and Coulter Counter Measurement", Analytic Chemistry, Vol 41, No 14, pp. 2017-2023, 1969

47. Raybech R M , "Determination of Particle Size Distribution of Isolated Non-metallic Inclusions in Steel", Pittsburgh Conference on Analytical Chemistry and Applied Spectroscopy, paper 63, 5 March 1967

48. Ihida M et al. , Trans. ISI Japan, Vol 6, pp. 31-38, 1966

49. Miyashita Y and Nishikawa K , Tetsu to Hagane, Vol 53, pp. 400, 1967

50. Guthrie R I L , "The Detection of Non-metallic Inclusions in Liquid Metals by a direct Method", in ref. 35, pp. 33-37, 1984

51. Mansfield T L , "Ultrasonic Technology for Measuring Molten Aluminum Quality", Light Metals, The Metallurgical Society of AIME, pp. 969-980, 1982

52. Mountford N D G and McLean A , "The Detection of Particles in Molten Iron Using a Pulsed Ultrasonic Technique", in ref. 35 pp. 97-98, 1984

53. Doutre D , "The Development and Application of a Rapid Method of Evaluating Molten Metal Cleanliness", PhD Thesis, McGill University, 1985

54. Berg R H , "Sensing Zone Methods in Fine Particle Size Analysis", Materials Research and Standarts, Vol 5, No 3, pp. 119-125, 1965

55. Coulter W H , "Means for Counting Particles Suspended in a Fluid", U. S. Patent No 112819, 20 Oct. 1953

56. Coulter W H , "High Speed Automatic Blood Cell Counter and Cell Size Analyser", Poceedings of the National Electronics Conference, 12, pp. 1034, 1956

57. Nakajima H , "Aqueous Modelling of Inclusion Behaviour in in Liquid Metals", MSc Thesis, McGill University, 1985

58. Tanaka S , PhD Thesis, McGill University, 1985

59. DeBlois R W and Bean C P , "Counting and Sizing of Sub-micron Particles by the Resistive Pulse Technique", Review of Scientific Instruments, Vol 41, No 7, pp. 909-915, 1970

60. Smythe W R , "Flow Around a Sphere in a Circular Tube", The Physics of Fluids, Vol 17, No 5, pp. 633-638, 1964

61. DeBlois R W ,Bean C P and Wesley R K A , "Electrokinetic Measurements with Sub-micron Particles and Pores by the Resistive Pulse Technique", J. of Colloid and Interface Science, Vol 61, No 2, pp. 323-335, 1977

62. Smythe W R , "Off-axis Particles in Coulter Type Counters", Review of Scientific Instruments, Vol 43, No 5, pp. 817-818, 1972

63. Davies R , Karuhn R and Graf J , "Studies on the Coulter Counter - Part II. Investigations into the Effects of Flow Direction and Angle of Entry of a Particle on both Particle Volume and Pulse Shape", Powder Technology, Vol 12, pp. 157-166, 1975

64. Kahrun R , Davies R, Kaye B H and Clinch M J , "Studies on the Coulter Counter - Part I. Investigations into the Effect of Orifice Geometry and Flow Direction on the Measurement of Particle Volume", Powder Technology, Vol 11, pp. 157-171, 1975

65. Spielman L and Goren S L , "Improving Resolution in Coulter Counting by Hydrodynamic Focusing", J. of Colloid and Interface Science, Vol 26, pp. 175-182, 1968

66. Lloyd P F , Coulter Counter Electronics Conference, 1968

67. Gregg E C and Steidley K D , Byophysical Journal, Vol 3, pp. 393, 1965

68. Eckoff R K , "Experimental Indication of the Volume Proportional Response of the Coulter-Counter for Irregularly Shaped Particles" J. of Scientific Instruments, Vol 44, pp. 648, 1967

69. Metals Reference Book, Ed. J. C. Smitthells, 5th ed., "General Physical Properties", pp. 948, Butterworths, Boston, 1976

70. The Industrial Graphite Handbook, Union Carbide Corporation, 1965

71. CRC Handbook of Materials Science, Ed. C. T. Lynch, Vol 2, CRC Press, 1975

72. Perry's Chemical Engineeres Handbook, 6th ed., pp. 5.15, McGraw Hill, 1973

73. Schenck H and Hinze H, Arch. Eisenhuttenw., Vol 37, pp. 545, 1966

74. Elliot J F , Gleiser M and Ramakrishna V , Thermochemistry for Steelmaking, Vol 2, Addison-Wesley, 1963

75. Bodsworth C and Bell H B , Physical Chemistry of Iron and Steel Manufacture, 2nd Ed. Appendix I, Longman, London, 1972

76. Fuwa T and Chipman J, Trans. AIME, Vol 212, pp.549, 1958

77. In ref. 75, pp. 383, 1972

78. In ref. 75, pp. 181, 1972

79. In ref. 72, pp. 5.34, 1973

80. Hultgren R , Desai P D , Hawkins D T , Gleiser M ,Kelly K K and Wagman D D , "Selected Values of the Thermodynamic Properties of the Elements", ASTM, 1973

81. Bader H , Gordon J R and Brown O B , "Thoery of Coincidence Count Correction for Optical and Resistive Pulse Particle Counters", Review of Scientific Instruments, Vol 43, No 10, pp. 1407-1412, 1972

82. Handbook of Fluid Dynamics, Ed. V. L. Streeter, 1st Ed. "Cavitation", pp. 12.1, McGraw Hill 1961

83. Geiger G H and Poirer D R , "Transport Phenomena in Metallurgy", pp. 67, Addison Wesley, 1972

84. Atkinson C M L and Wilson R , "Artefact Peaks in Particle Size Distributions Measured by the Electrical Sensing Zone (Coulter Counter) Method, Powder Technology, Vol 34, pp. 275-284, 1983

85. Wilson R , "Calculation of the Electric Field Within an Electrical Sensing Zone Counter", Particle Characteristics Vol 1, pp. 37-43, 1984

86. Scott W T , The Physics of Electricity and Magnetism, 2nd Ed., pp. 212, John Wiley, New York 1966

87. Doutre D , Research Laboratories, Alcan Corp., personal communication, 1985

88. Maxwell J C , "A Treattise on Electricity and Magnetism", Vol 1, 3rd Ed., pp. 440, Clarendon Press, Oxford, 1904

89. Peirce B O , "A Short Table of Integrals", 4th Ed., pp. 68, Blaisdell, 1956

LIST OF FIGURES

Figure 16	10 second counts on the MCA with the modified probe, ca. 8 grams of steel sample. Only 3 counts above channel 60 corresponding to a ca. 17 micron inclusion size are visible.
Figure 17	Microstructure of the 3% Si, 5% B steel showing the globular borosilicate inclusions.
Figure 18	Microstructure of the same steel after etching in 2% nital. Glassy borosilicate inclusions are still visible at the background.
Figures 19 and 20	Scale found around the probe, electrode and the inner crucible wall after 0.2% aluminum addition.
Figure 21	Resistive pulse signals in silicon-boron steel after aluminum addition, sampling under 20 amperes, with a 400 micron orifice.
Figure 22	Associated 10 second counts on the MCA after aluminum addition, ca. 13 gram steel sample.
Figure 22-A	Size distribution of inclusions in a silicon boron steel after 0.1% Al addition. Calculation is based on the MCA image in Figure 22 and conversion from resistive pulses in microvolts to particle sizes in microns is made via Figure 3-A.
Figure 23	Orifice Stability after the silicon-boron steel experiment with aluminum addition.
Figure 24	Microstructure of the 3% Si, 5% B steel after 0.1% Al addition.
Figure 25	Unstable baseline, (A) upward spikes usually associated with unsteady current, (B) oscillatig baseline.
Figure 26	Baseline oscillations in mercury associated with high flow rate.
Figure 27	Cross-section of a 300 micron orifice, flame drilled and polished into the side of a Kimax culture tube as used in LiMCA measurements.
Figure 28	Free energy change associated with the reaction (15).
Figure 29	A typical resistive pulse signal obtained while aspirating cast iron through a 300 micron orifice and passing a cuurent of 20 amperes.
Figure 30	Skewed pulses obtained with a sharp edged entry and the effect of background noise during initial filling.

LIST OF TABLES

Table II.1	Conversion of total oxygen and sulphur, ppm, into volume fraction of inclusions Vf, ppm.
Table II.2	Comparison of the frequency distribution of inclusions in experimental aluminum killed steels in Figure II.2 (46) and equation (32).
Table II.3	Comparison of the frequency distribution of inclusions in a commercial aluminum killed steel, steel (D) in Figure II.2 and equation (32).